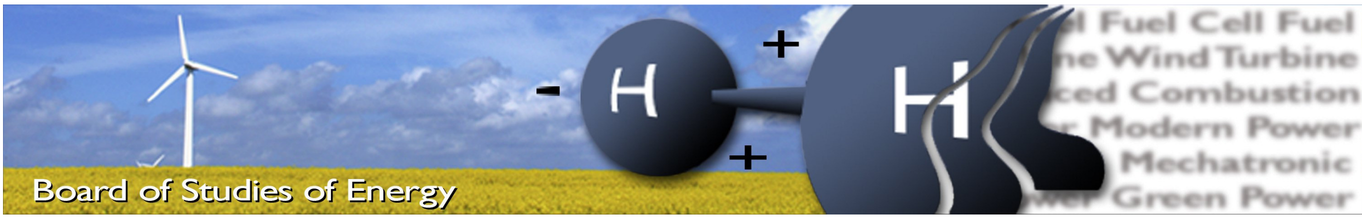

Title: Integration of a Battery Energy Storage System in a Photovoltaic Cascaded H-Bridge Inverter
Semester: 10th
Semester theme: Master Thesis
Project period: 01.02.19 to 31.05.19
ECTS: 30
Supervisor: Remus Teodorescu & Dezso Séra
Project group: PED4-1044

Chiara Sirico

SYNOPSIS:

The intermittent nature of the solar power and partial shading phenomena represent the main challenges for PV inverters. In order to cope with these issues, in this project two hybrid PV-BESS topologies for a single cell of a CHB inverter are proposed. By means of numerical analysis, their efficiencies and performances under different levels of irradiance are compared. Finally, the benefits of a battery energy storage system on a PV-CHB inverter, when the cells are operating under unbalanced irradiance conditions, are shown.

Pages, total: 59

By accepting the request from the fellow student who uploads the study group's project report in Digital Exam System, you confirm that all group members have participated in the project work, and thereby all members are collectively liable for the contents of the report. Furthermore, all group members confirm that the report does not include plagiarism.

Summary

Nowadays, the increasing environmental awareness have led to a substantial growth of photovoltaic systems. Traditionally, several PV modules are arranged in order to build a string or an array, which are then interconnected to the grid by means of a 3-level voltage source inverter. However, the intermittent nature of the solar power and partial shading phenomena may have a negative impact on the global production and can lead to disturbances on the grid side. For this reason, in order to enhance the dispatchability of the solar energy resources and to provide auxiliary services, PV systems are often coupled with battery energy storage systems (BESS). A solution which suits best with this application is represented by the exploitation of a Cascaded H-Bridge (CHB) inverter, in which every sub-module can be connected to an independent power generator. Furthermore, different power levels can be achieved thanks to the inherent modularity of this architecture, without affecting the sizing of the switching devices.

In this project, with the aim of integrating a BESS in the PV-CHB architecture, two modular PV-BESS topologies are proposed. Both a PV module and a BESS are interfaced with a single sub-module capacitor of the CHB. The main difference concerns the way of interconnection of the BESS module to the sub-module dc-link: in one case the BESS is controlled by means of an individual bidirectional dc-dc converter; whereas, in the second case, the BESS is supposed to be directly in parallel with the sub-module capacitor. In both cases, the PV module is decoupled by the common dc-link by means of a boost converter, in order to track the maximum power operation point.

The project consists of the following phases. Firstly, the modelling of the two proposed systems has been developed and all the operation modes investigated, in order to properly design the control strategy. Secondly, a numerical analysis has been carried out on PLECS®, in order to verify the feasibility of the control and to investigate about the main differences between the two topologies. In particular, the comparison is focused on the efficiency under different irradiance levels and on the European efficiency, which takes into account a typical daily operation of the system. Results show that the additional dc-dc power conversion stage leads to a significant reduction of the global efficiency. On the other hand, it provides a better control of the battery current, which also results in a limitation of the battery internal losses.

Although the topology which does not exploit the additional dc-dc power stage results to be beneficial from the efficiency point of view, a proper control strategy for the CHB shall be designed, in order that all the battery modules always operate in safety conditions. However, this matter proved to be challenging, and thus the topology with the additional dc-dc conversion stage has been considered in order to verify the benefits of the BESS under partial shading conditions.
The tested system consists of a CHB inverter. Each sub-module is connected to an hybrid PV-BESS module. In particular, an MPPT control, based on the Perturb & Observe technique, has been implemented in order to independently track the MPP of each PV module. The BESS module is interfaced by means of a bidirectional dc-dc converter, which regulates the battery current in order to compensate the mismatch

between the output power reference and the PV generation. The CHB is driven in order to control the grid current, according to the nearest level control (NLC) modulation. Furthermore, a sorting algorithm has been implemented in order to keep balanced the voltages across the SM capacitors. It has been proved that the output grid power remains unchanged when the irradiance level on a single panel sharply drop. However, the control strategy implemented leads to SOC unbalances among the sub-modules.
Further researches shall investigate about a sorting algorithm based on SOC, in order to enhance the permanent operation of the proposed architecture.

Contents

List of Acronyms

AC Alternating Current

BESS Battery Energy Storage System

CCM Continuous Conduction Mode

CHB Cascaded H-Bridge

DC Direct Current

DER Distributed Energy Resources

ESR Equivalent Series Resistance

IGBT Insulated Gate Bipolar Transistor

MMCC Modular Multilevel Cascaded Converter

MPP Maximum Power Point

MPPT Maximum Power Point Tracking

NOCT Nominal Operating Cell Temperature

PCC Point of Common Coupling

P&O Perturb and Observe

PI Proportional Integral

PR Proportional Resonant

PV Photovoltaic

PWM Pulse Width Modulation

RMS Root Mean Square

SAM System Advisor Model

SOC State of Charge

SOH State of Health

STC Standard Test Conditions

TSO Transmission System Operator

VSI Voltage Source Inverter

Chapter 1

Introduction

In this chapter the background and the motivation of the project are presented. Finally, the project objectives and the limitations are listed.

1.1 Background

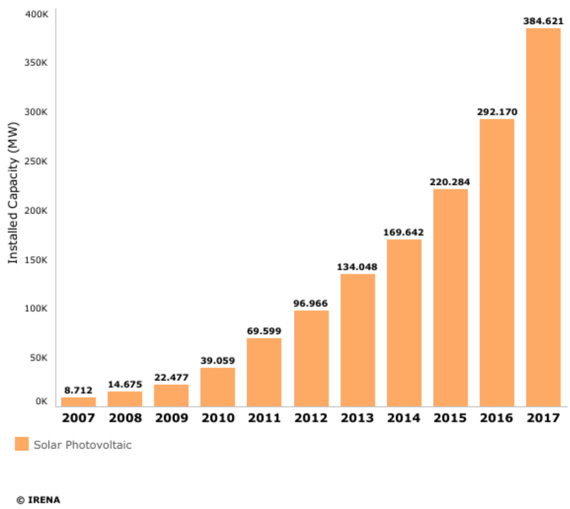

Figure 1.1: Evolution in PV Installed Capacity [1].

The ongoing growth in energy demand and the increasing environmental awareness have strengthened the need to integrate renewable energy resources into the traditional power systems. In particular solar photovoltaic systems have experienced an exponential growth during the last decade, thanks to incentive programs proposed by local governments. According to the Global Market Outlook 2018-2022 provided by SolarPower Europe [2], in 2017 the global cumulative solar power installed was approximately 400 GW. In only 10 years the world's total PV capacity increased by over 4300%, from around 9 GW in 2007. In particular, a total of 99.1 GW of grid-connected solar power was installed only in 2017. The Figure 1.1 shows the evolution of global installed PV capacity over the last decade, according to the data freely provided by IRENA [1]. It is worth considering that more than 99% of the total capacity is represented by grid-connected PV systems. For this reason, hereafter the focus will be placed on these latter.

1.1.1 Overview of grid-connected photovoltaic generation systems

Grid-connected PV power generation systems can be found in different sizes and power levels in order to fit different needs and applications, ranging from a few hundreds of Watt for a single PV module, to hundreds of MW for the biggest PV plants. Certainly, the key element of a grid-connected photovoltaic generation is the power converter. It has the main function of regulating the output currents injected into the grid, in order to meet the requirement of the utility grid codes. Its second role is to maximize the extraction of power from the PV generators. Since solar panels are characterized by a complex non-linear relationship between voltage and the generated power, a proper Maximum Power Point Tracking (MPPT) algorithm must be used, in order to optimize the generation. Grid-connected PV converters can be commonly subdivided in centralized, string, multi-string and AC-module topologies, depending on the PV module arrangement, as shown in Figure 1.2 [3]. It is worth pointing out that a series connection of PV modules is known as string and more strings can be connected in parallel by means of string diodes, in order to create an array .

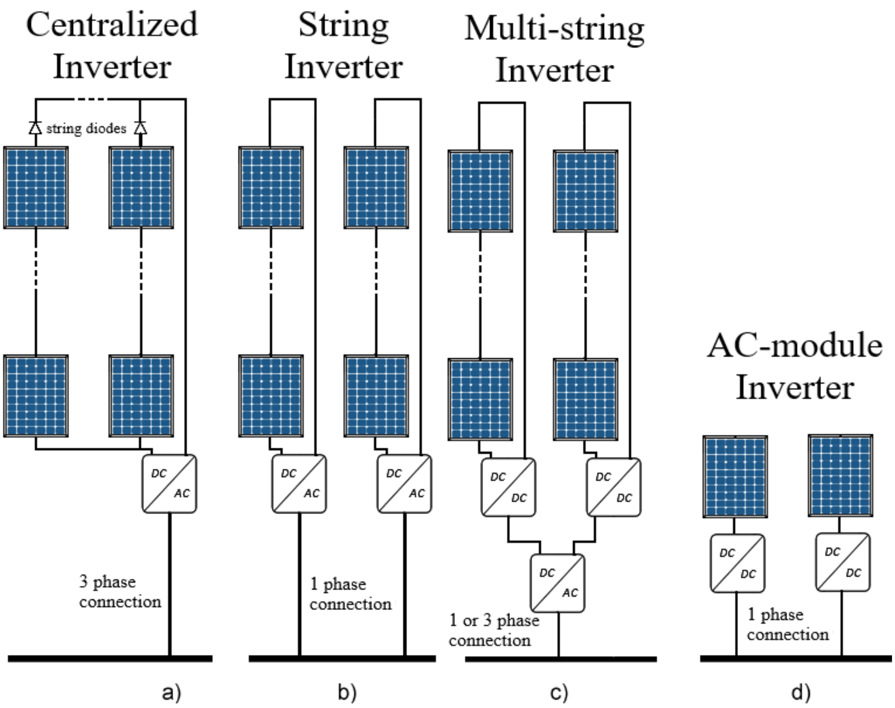

Figure 1.2: Inverter configurations for PV system.

- Centralized inverter: A single 3-level voltage source inverter (VSI) interfaces a whole PV array to the grid. This configuration can only provide a single MPPT operation, and under unbalanced irradiation or temperature conditions among the PV modules, mismatch losses are generated. Nevertheless, this topology is still the most common for large-scale PV plants (500 kW-10MW), due to its high efficiency and simple-structure.
- String inverter: a single PV string is connected to the grid by means of its own

inverter. In this topology the global losses are reduced compared to the centralized inverter, because there aren't conduction losses associated with string diodes and the MPPT algorithm is individually performed on each string. This arrangement is commonly used for small-medium scale plants (up to 10 kW).

- Multi-string inverter: several strings are interfaced with their own dc-dc converter to a common dc-ac inverter. This approach is also known as power optimizer, since a distributed MPPT algorithm is performed. This topology suits to a wide range of power, thanks to its flexibility and high efficiency.

- AC module inverter: is the integration of the inverter and a single PV module into one electrical device. It nullifies the mismatch losses between PV modules since each PV module performs an independent MPPT. This configuration is also known as microinverter because of the small size and low power rating (up to 350 W). Typically, due to the low voltage of PV modules, this configuration requires an additional dc-dc stage in order to elevate voltage, which affects the system efficiency.

As a result of the huge growth which concern PV generation, nowadays an increasing effort is put to realize more complex power converters topologies, in order to increase efficiency, power extraction, power density and reliability, without impacting on the cost [4].
One interesting solution, either for medium or low voltage systems, is represented by the exploitation of multilevel converters for PV application. The main benefit of the multilevel voltage-source converters is that they can generate an output voltage waveform that has a greater integer number of levels, with respect to the traditional two-level voltage source converters. As a direct result, the output waveform has a reduced total harmonic distortion (THD). In addition, the effective switching frequency of the output waveform is higher than the switching frequency of a single semiconductor device. As a result, the size of the grid connection filter can be reduced, for a given switching stress. Finally, the use of multilevel converters can lead to the avoidance of the bulky transformer, usually needed to raise the voltage and realize a proper interconnection with the grid.
Among different families of multilevel inverters, the modular multilevel cascade converter (MMCC) has become more and more attractive for photovoltaic application, given its inherent modularity. MMCC shows a per-phase circuit configuration based on the series connection of converter elements, called sub-modules, typically consisting of a full-bridge or a half-bridge. This arrangement allows to reach higher voltage levels by exploiting semiconductor devices of lower voltage rating. The modularity provides several advantages. Firstly, fault tolerance is improved, since a possible faulty module can be by-passed and the whole system can still operate with reduced output voltage level. Secondly, modularity leads to reduce maintenance costs and facilitates the replacement of a faulty cell. In particular, between different MMCC topologies, the focus will be placed on Cascaded H-Bridge (CHB) in this work. In the CHB architecture, power sources of different sizes can be interlinked. This suits best for PV applications.

1.1.2 Integration of battery energy storage systems in grid-connected PV systems

One of the main challenges posed by the high penetration of PV energy resources into the traditional power system is represented by the intermittent nature of the supplied power. It was stressed that PV systems are connected to the utility grid by means of power converters, that have different characteristics with respect to the conventional interfaces of traditional thermal generation plants. Indeed, while the steam and hydro turbines enable the control of the supplied power, through the regulation of the inlet valve, the PV generation is intermittent and unpredictable, due to the stochastic nature of the solar irradiation and the environmental temperature. Moreover, the rotating machines inherently provide inertia to the system, by improving the stability of the grid. On the contrary, the low-inertia which characterizes the PV generator can lead to stability issues resulting from great variations in the power demand. If no actions are taken in these regards, the PV plant might be required to curtail the production from the Transmission System Operator (TSO).

Latest studies, as referred in [5] and [6], are trying to develop PV multilevel inverters with additional energy storage capability, in order to mitigate the negative impact of PV generation on the grid, by smoothing the abrupt changes of the generated PV power. Furthermore, ancillary services could be provided to the utility grid.

Among different energy storage technologies, batteries have gained more attention and application due to scalable power rating, lower cost, non-polluting and high reliability and efficiency. Battery energy storage system (BESS) acts as an energy buffer in the PV generation system and offers several advantages.

Firstly, it enhances the self-consumption of residential PV plants, by storing the energy when it is not demanded by local loads and by supplying this energy when required. Secondly, it provides some services to the utility grid, such as frequency and voltage regulation, peak shaving and load shifting [4]. Finally, the integration of a BESS into the PV converter can also cope with the PV power oscillations, by limiting the ramp rate of the power injected into the grid.

As a result, these hybrid PV-BESS systems allow a better exploitation of Distributed Energy Resources (DER), improve the dispatchability of PV resources, enhance the efficiency and stability of the overall system and provide operational flexibility and continuity of power supply in case of a failure.

1.2 Current status of hybrid PV-BESS systems and project motivations

The conventional PV-BESS system for utility-scale applications is shown in Fig.1.3. The PV and the BESS systems are independently connected to a low voltage point of common coupling (PCC) by means of a traditional two-level centralized converter. Furthermore, a bulky step-up transformer is needed, in order to realize the connection with the medium voltage grid.

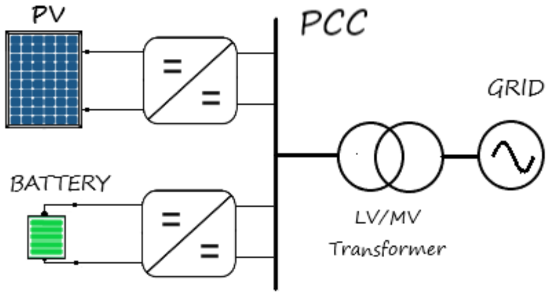

Figure 1.3: Conventional two-level PV-BESS.

Hybrid PV-BESS converters can already be found as a commercial product for household applications (e.g. SE5000-XXS by SolarEdge) [7].
Nowadays the research about grid-connected PV systems is focusing on MMCC, due to the aforementioned benefits they can provide, concerning losses, extracted power, size and fault-tolerance. Nevertheless, MMCC-based hybrid PV-BESS systems aren't still available and can only be found as experimental prototypes, specifically for medium-high voltage application, as described in [5], [6] and [8].
In this project the advantages of BESS integration into a grid-connected PV CHB-based single-phase system will be investigated. In particular, the interest is directed to improving the performance of the system in Fig.1.4, which is dealt with in [9] and [10]. As can be noticed by looking at the Fig. 1.4, the single-phase CHB inverter achieves a direct dc-ac energy conversion between the PV sources and the utility grid, and it is characterised by a simple modular structure.
The CHB converter consists of N full-bridge sub-modules connected in series. Each sub-module is used as interface with a PV module or string, which is an independent power generator. In order to maximize the overall solar power production, every dc-link voltage should individually track the MPP voltage of the corresponding PV module. With this goal, the control strategy proposed in [9], [11] and [10] performs a distributed MPPT algorithm among the cells, by mixing the staircase modulation and the pulse width modulation (PWM). The main idea is that only one cell at time is on PWM mode, while the others can be either connected or bypassed. The selection of the switching state of each cell is made by means a special sorting algorithm. Experimental results have shown that this control strategy is able to enhance the MPPT efficiency under unbalanced irradiance conditions among the PV modules.
Nevertheless, in case of deep or enduring mismatches, shaded panels seriously affect the power generation of the others modules in the CHB architecture. To overcome this issue, the two-stage conversion system should be used. As it is shown in fig. 1.5,

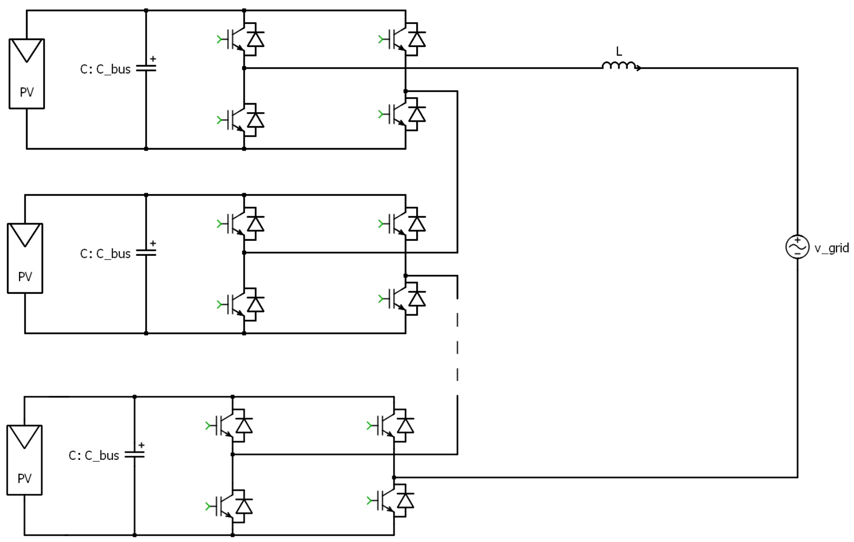

Figure 1.4: Single-phase, single-stage, grid-connected PV CHB inverter

each cell of a two-stage CHB topology consists of a PV module and a dc-dc converter. The additional dc-dc stage decouples the PV operating point from the inverter grid current control. Hence, each cell is able to perform an independent MPPT control. As a drawback, the number of switching devices is increased significantly, by affecting the cost, the reliability and the efficiency of the entire system.

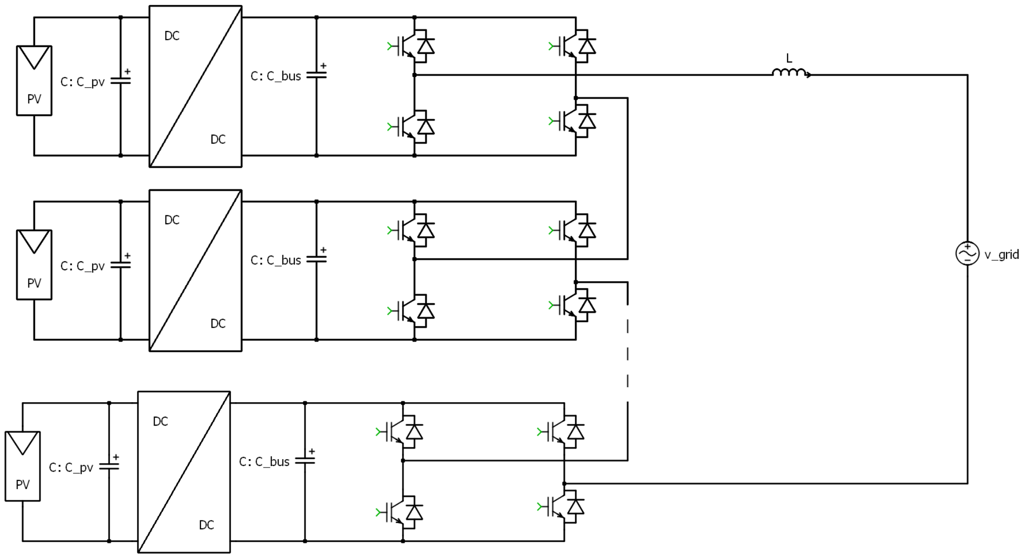

Figure 1.5: Single-phase, two-stage, grid-connected PV CHB inverter

In order to take full advantages from this architecture, the integration of a BESS unit at sub-module level is proposed. In this way the system will be able not only to perform a distributed MPPT under deep uneven conditions, but also to compensate the power losses caused by partial shading phenomena. Furthermore, the integration of a BESS in the PV system provides all the aforementioned advantages for dispatchability of intermittent PV power generation. As a result, the negative impact of PV generation on the utility grid is reduced.
In particular, two hybrid PV-BESS cell topologies are proposed, as shown in Fig.1.6.

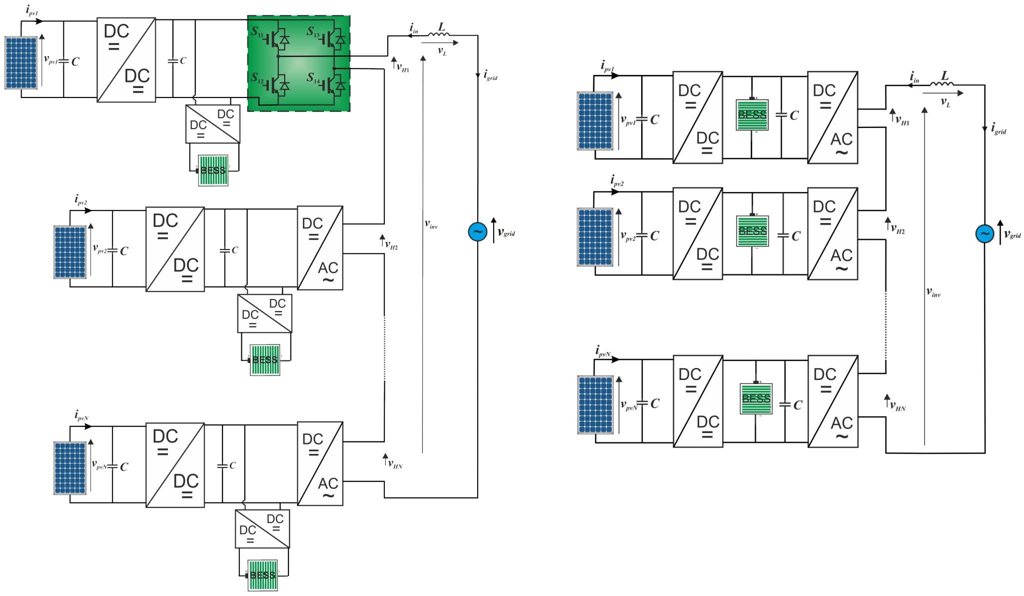

(a) (b)

Figure 1.6: Proposed PV-BESS cell topologies.

By looking at the fig.1.6, it can be noticed that, in both cases, the interface between the PV module and the sub-module dc-link is realized through an uni-directional dc-dc boost converter, which main task is to perform an individual MPPT. Hence, it is clear that the major difference between the two topologies concerns the way in which the battery module is connected.
In the topology in fig. 1.6.(a), a bi-directional dc-dc converter decouples the battery from the common dc-link and properly manages the charging and discharging processes, by controlling the battery current.
On the contrary, in the topology in fig. 1.6.(b) the battery is directly connected to the sub-module dc-link. In this case, the battery current can't be directly controlled and the value voltage at the dc-link is strictly related to the battery voltage.

1.3 Project Objectives and limitations

This project main objective is to investigate how a battery energy storage system can be integrated in a single-phase grid-connected PV CHB-based system. The BESS will enhance the overall performance of the system, with a particular focus on the operation under partial shading conditions.
With this aim, the following steps are planned:

- Two PV-BESS cell configurations are proposed and they will be properly modelled and sized.
- All the possible operation modes of the hybrid PV-BESS subsystem will be investigated in order to design a suitable control strategy. After that, the feasibility of the control strategy will be tested by means of the simulation tool PLECS®.
- A comparison between the two topologies will be carried out, by looking at the operating conditions of the battery and at the global efficiency.
- The benefits of the addition of a BESS in the CHB inverter for PV application will be tested.

On the other hand, the following limitations have been set:

- The simulation concerning the comparison between the two topologies is restricted at the sub-module level.
- In the comparison the economic aspects, such as the overall cost, and the reliability of the entire system will not be included.
- The feasibility of the proposed architecture and of its control strategy will not be validated by building a laboratory prototype, but only on a simulation environment.
- Although the proposed architecture fits well for high power systems, which would consists of a significant number of cells, for the sake of simplicity, a typical low power single-phase residential PV system will be considered.
- In order to perform the MPPT, a *P&O* algorithm will be used. Others high-performance MPPT strategies will not be investigated.

Chapter 2

Modelling of the System

In this chapter the operating principle, the modelling and the sizing of the main components of the system will be developed. In particular, the small signal models of the power converters interfacing the PV and the BESS with the common dc-link will be obtained, as a prerequisite for the design of the corresponding controller.

2.1 Photovoltaic Module: Operating Principle and Modelling

A PV cell is a semiconductor device able to convert solar energy into electrical energy by exploiting the photovoltaic effect.
Nowadays, the most widely used solar cell is made of crystalline silicon (Si). A PV cell mainly consists of a large p-n semiconductor junction. The p-layer contains an abundance of holes, whereas the n-layer has an excess of electrons. As a result, a depletion region with an internal electric field is generated, due to the migration of electrons into the p-layer and of holes into the n-layer.
When a photon with sufficient energy, such as the sunlight, hits the material, an electron is excited and enters in the conduction band, leaving a hole in the valence band. Under the force applied by the internal electric field, electrons migrate toward the cathode, while holes are concentrated near the anode.When the device is closed on an electric path, the electrons will move from the cathode towards the anode, to fill the holes that are concentrated there. As a result, a DC current is generated.
Nevertheless, a single solar cell can produce a maximum open circuit voltage of about 0.5 V. For this reason, a PV module consists of a certain number of series-connected solar cells, typically from 36 up to 72, in order to reach a higher voltage level in line with the voltage requirements of common loads.

A PV panel can be modeled by means of the equivalent electric circuit shown in Fig.2.1. The current generated by the incident light, known as photoelectric current I_{ph}, is modeled as a current source. Whereas, the p-n junctions is represented by a diode, characterised by the ideality factor n and by the reverse saturation current I_o. In order to realize a more realistic model, losses are taking into account through two parasitic resistances, a series resistance R_s and a parallel resistance R_p.
A detailed description of the PV panel model will be now provided [12].
The model adopted is also known as *5 parameters model* because, in order to be

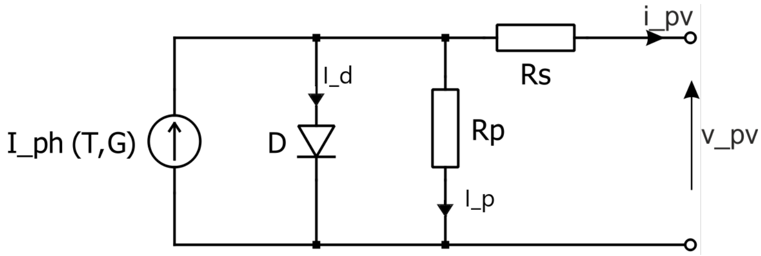

Figure 2.1: Equivalent circuit of a PV module.

implemented, it requires the definition of the following 5 parameters: I_{ph}, I_o, n, R_s, R_p.
By taking a closer look at the circuit shown in Fig. 2.1 and by applying the Kirchhoff's Current Law, it follows that the output current from the panel is:

$$I_{pv} = I_{ph} - I_d - I_p \tag{2.1}$$

The diode current can be expressed as the following exponential function:

$$I_d = I_o \Big[\exp \frac{V_{pv} + I_{pv} R_s}{n V_T} - 1 \Big] \tag{2.2}$$

where V_T represents the junction thermal voltage:

$$V_T = \frac{N_s k T}{q} \tag{2.3}$$

It is important to highlight that the photocurrent and the diode reverse saturation current are affected by the solar irradiance level and the solar cell temperature, as:

$$I_{ph} = \frac{G}{Gn} \Big[I_{scn} + K_i (T - T_n) \Big] \tag{2.4}$$

$$I_o = \frac{I_{scn} + K_{Isc}(T - T_n)}{\exp\left(\frac{V_{ocn} + K_v (T - T_n)}{n V_T}\right) - 1} \tag{2.5}$$

In summary, according to the five parameters model, the relationship between the current and the voltage of a PV module can be expressed as:

$$i_{pv} = \frac{G}{Gn} \Big[I_{scn} + K_i (T - T_n) \Big] - \frac{I_{scn} + K_{Isc}(T - T_n)}{\exp\left(\frac{V_{ocn} + K_v (T - T_n)}{n V_T}\right) - 1} \Big[\exp \frac{V_{pv} + I_{pv} R_s}{n V_T} - 1 \Big] - \frac{v_{pv} + i_{pv} Rs}{R_p} \tag{2.6}$$

In order to simulate a realistic component, the PV module TSM-335 PD14 by Trina Solar has been selected. The module consists of $N_s = 72$ series-connected cells, each of which covers an area of $(156.75 \times 156.75)\, mm^2$. Therefore, the total area of the PV module is $A = 1.77\,\mathrm{m}^2$.
The data provided by the manufacturer at Standard Test Conditions (STC) (i.e. Irradiance $G_n = 1000\,\mathrm{W/m^2}$; Cell Temperature $T_n = 25\,°\mathrm{C}$; Air Mass = AM 1.5) and at Nominal Operating Cell Temperature (NOCT) (i.e. Irradiance = $800\,\mathrm{W/m^2}$; Ambient Temperature = $20\,°\mathrm{C}$; Wind speed = $1\,\mathrm{m/s}$) are shown in Tab.2.1.
Unfortunately, not all the parameters required for the modelling can be found on the datasheet and they should be extracted with cumbersome procedures.

Data at STC	**Value**
Maximum Power (P_{MPPn})	335 W
Maximum Power Voltage (V_{MPP})	37.6 V
Maximum Power Current (I_{MPP})	8.91 A
Open Circuit Voltage (V_{ocn})	46.0 V
Short Circuit Current (I_{scn})	9.35 A
Module Efficiency (η_{m})	17.2 %
Data at NOCT	**Value**
Maximum Power (P_{MPP})	249 W
Maximum Power Voltage (V_{MPP})	34.8 V
Maximum Power Current (I_{MPP})	7.14 A
Open Circuit Voltage (V_{oc})	42.6 V
Short Circuit Current (I_{sc})	7.55 A
Temperature Coefficients	**Value**
Temperature Coefficient of P_{MPPn} (K_p)	−0.41 %/K
Temperature Coefficient of V_{ocn} (K_v)	−0.32 %/K
Temperature Coefficient of I_{scn} (K_i)	0.05 %/K

Table 2.1: Parameters of the PV module.

For the sake of simplicity, the missing parameters have been obtained from the *CEC Modules* Database provided by the last version of the NREL-System Advisor Model, SAM 2018.11.11 [13]. These last are shown in Tab. 2.2. Therefore, the diode ideality factor at STC is given by:

$$n = \frac{aq}{kN_sT_n} = 0.95351$$

where k is the Boltzmann constant and q is the electron charge.

SAM PV parameters	Value
Ideality factor (a)	1.764 38 V
Series resistance (R_s)	0.342 502 Ω
Parallel resistance (R_p)	454.368 Ω

Table 2.2: SAM parameters of the PV module.

On the basis of the datasheet parameters and the SAM parameters, the PV module has been implemented on PLECS® as a current source $I_m = I_{ph}(T,G) + I_d(T,V_{pv},I_{pv})$, a series resistance R_s and a parallel resistance R_p.
The accuracy of the model has been tested by noticing that the power-voltage and current-voltage characteristics for different levels of irradiance, as shown in Fig.2.2, perfectly fit with the curves provided by the manufacturer.

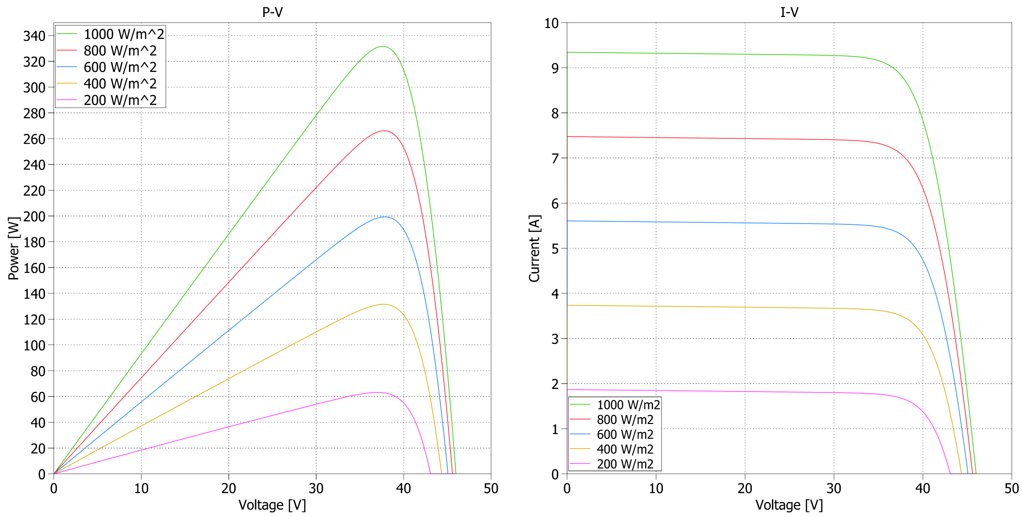

(a) (b)

Figure 2.2: PV characteristic curves.

2.2 DC-link Capacitor

The dc-link capacitor is supposed to be real and, therefore, it has been modelled as an ideal capacitor in series with its Equivalent Series Resistance (ESR).
The dc-link capacitor is sized according to the Eq.2.7, in order to achieve a maximum desired amplitude of the voltage ripple $\hat{v}_{dc}$ across the capacitor [3].

$$C = \frac{P_{pv}}{2\omega_{grid} V_{dc} \hat{v}_{dc}} \tag{2.7}$$

From the calculation results that a capacitor of 4.7 mF is needed in order to keep the dc-link voltage ripple under the 5 % of its average value.
For an electrolytic capacitor of that size the ESR is equal to 65 mΩ.

2.3 Battery Pack: Operating Principle and Modelling

A battery is an electrochemical device which converts chemical energy into electrical energy. The process can be reversed for the rechargeable batteries, such as the ones suitable for energy storage application. Traditionally, a battery consists of several cells stacked together. A cell is the building block where the electrochemical reaction takes place. It basically consists of an electrolyte placed between two electrodes of different polarities, the anode and the cathode.
A chemical reaction, depending on the technology of the battery and involving the electrodes and the electrolyte, gives rise to cations (positive ions) and anions (negative ions). The electrolyte enables the flow of ions and at the same time inhibits the flow of electrons.
As a result, depending on the concentration of the electrolyte, a certain electromotive force is generated between the terminals of the cell. The latter is also known as "open-circuit voltage", and represents the existing voltage at the terminals when the

cell is disconnected from any external circuit. The open-circuit voltage generated by a single cell is usually of few volts. In order to reach the desired voltage rating, more cells must be connected in series.
On the other hand, when the terminals are closed on an external circuit, the electrons flow under the action of the electromotive force and a DC current is generated. In order to obtain the desired current rating many cells should be connected in parallel. However, parallel connections between cells are not recommended because even small unbalances in voltages generates undesired currents.

The most meaningful parameter to look at, in order to find the proper size of the battery pack, is the capacity of the battery.
The battery capacity C represents the total amount of electric charge that can be supplied from a fully charged state. The traditional unit for the battery capacity is the ampere-hour, where $1\,\mathrm{Ah} = 3600\,\mathrm{C}$, according to the SI. Generally, the battery capacity depends on the discharging current. In particular, it is curtailed with higher discharging current rate. For this reason, the capacity is specified along with a current rate. For example, if C rate is the current rate in ampere (i.e. A current of C A will discharge the battery in $1\,\mathrm{h}$), then nC rate will discharge the battery in $1/n$ hours [14]. However, for the sake of a simple modelling, the battery capacity is assumed to be constant even under variable discharging current rate.

It is now worth pointing out the definition of other parameters of interest: the state of charge and the energy stored.
The State of Charge (SOC) is a measure of the residual capacity of the battery. It is defined in the equation 2.8, where Q_o is the total charge that the battery can store and i_b is the discharging current.

$$SOC(t) = SOC(t_0) - \frac{\int_{t_0}^{t} i_b d\tau}{Q_0} \tag{2.8}$$

On the other hand, the energy stored in a battery depends on the voltage at the terminals and on the amount of stored charge, as shown in Eq.2.9. The traditional unit for the energy is the watt-hour, where $1\,\mathrm{Wh} = 3600\,\mathrm{J}$, according to the SI.

$$E = V \cdot C \tag{2.9}$$

The most popular technologies used for energy storage systems are the lead acid and the Li-ion batteries. The lead acid battery is the pioneer technology for energy storage application. It is widespread on the market thanks to the low cost and high safety features. Whereas, the Li-ion batteries are characterised by higher efficiency, longest lifetime and higher power density, but they require particular regulatory system to monitor that any over-charging or over-discharging phenomena occur. These latter can seriously damage the battery, resulting in safety hazards [14]. As a result, the price of Li-ion battery is still not in a competitive position on the market with respect to lead acid batteries.

It is well known that realizing a reliable battery model is difficult, due to the dependency of the battery performance on several parameters, some of which are really hard to specify. For example, the State of Health (SOH) of the battery, that represents the performance of the battery compared to its specifications, is affected by the age and by the way the battery has been used in the past. Since these latter can't be easily specified, the SOH must be evaluated with some cumbersome procedures. Nevertheless, the simplest model shown in Fig. 2.3 suits our purposes well, and thus it has been implemented for the simulation. The equivalent circuit of the battery consists of an ideal voltage source, which provides the open-circuit voltage V_{oc}, in series with a constant internal resistance R_{int}.

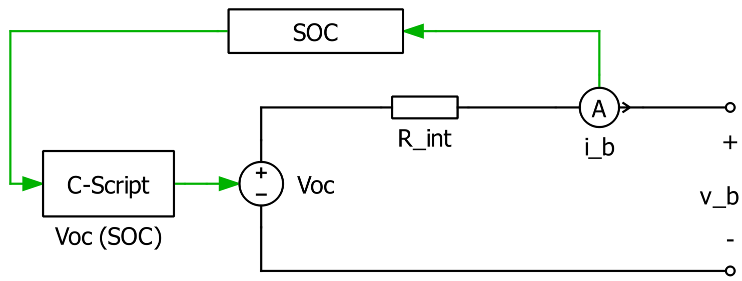

Figure 2.3: Equivalent circuit of the battery.

In general, both the voltage source and the resistance are affected by the SOC and the temperature. For the sake of simplicity, only the dependency of the open-circuit voltage on the SOC will be taken into account.
The effective relationship between V_{oc} and SOC depends on the chemistry of the battery and it is usually provided by the manufacturers by means of the discharging curves.
However, the non-linear pattern between V_{oc} and SOC can be qualitatively yielded as shown in Eq. 2.10, where E_o is the standard potential of the battery, R is the ideal gas constant, T is the absolute temperature and F is the Faraday constant [14].

$$V_{oc} = E_o + \frac{RT}{F}\log(\frac{SOC}{1-SOC}) \tag{2.10}$$

With the aim to find the perfect size for the battery that should be matched with the PV module, it is important to fix the voltage and the capacity, in such way that the available energy fulfills the purpose.

With reference to the choice of the nominal voltage, it is worth to make a few comments. At sub-module level it is logical to keep the dc-link voltage at a higher level than the panel voltage, which maximum value is represented by the open circuit voltage. In fact, in order to inject the active power into the grid, is required that the inverter output voltage is sufficiently higher than the grid voltage peak value.
As a consequence, for what concerns the topology in fig.1.6(b), where the battery is directly connected to the dc-link, a reasonable value for the nominal voltage of the battery pack is the classical 48 V.

By contrast, in the topology shown in fig.1.6(a), the exploitation of a bidirectional dc-dc converter interfacing the battery pack with the dc-link, offers more flexibility for what concerns the choice of the the battery pack voltage. In fact, it is possible to scale down the nominal voltage of the battery, while keeping the dc-link voltage at a sufficiently high level, by properly sizing the inductor of the dc-dc converter. However, in order to make a reasonable comparison between the two proposed topologies,

the same battery pack will be used in the simulation.
It is clear that the voltage at the dc-link can't be the same for the two topologies. In fact, in the topology in fig. 1.6(b), the dc-link voltage is strictly dependent by the battery voltage and, therefore, it assumes values near the 48 V.
Whereas, in the topology in fig.1.6(a), the dc-link voltage must always be higher then the battery voltage. This is a necessary condition for the good operation of the battery current control. During the simulation the reference for the dc-link voltage has been set at 51 V, in order that this requirement is always fulfilled.
Once the battery pack voltage has been decided, the capacity of the battery is chosen by estimating the amount of energy that the battery is called to stored, according to the Eq.2.9.
For the purpose of compensating for partial shading and providing some ancillary services, the energy that the battery should store is supposed to be half of the daily PV production.
A preliminary evaluation of the daily production of the selected PV panel has been done by means of the interactive tool provided by the Photovoltaic Geographical Information System (PVGIS) [15]. The PV panel is supposed to be mounted in Aalborg, north Denmark. In Fig.2.5 the daily average global irradiance in the month of June is shown. The results of this calculation consist of hourly values of the average solar irradiance for the chosen month.

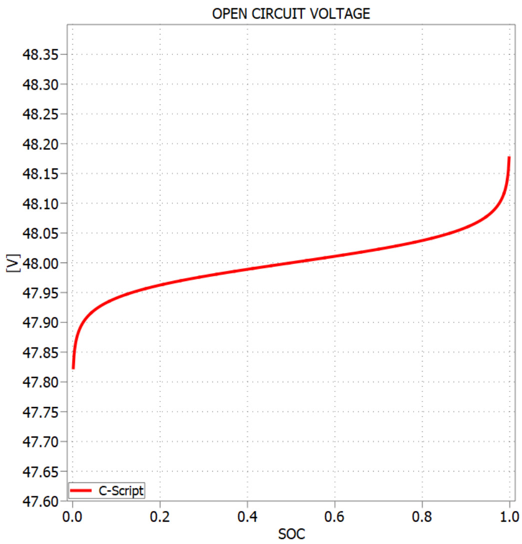

Figure 2.4: Battery V_{oc} charging curve.

With reference to the daily irradiance profile, the daily energy production of the selected PV module has been evaluated as follows:

$$E = A \times \eta_m \times \int_{day} G(t)\, dt \tag{2.11}$$

Where A is the area covered by the PV module and η_m its efficiency.
A daily production of 1.8 kWh results from the calculation.
According to the Eq.2.9, in order to store the half of the daily production by means of a 48 V battery, a capacity of about 20 Ah is needed.
The lithium iron phosphate (LiFePO4) Li-Ion battery cell LFP3.2V/20AH, produced by LIYUAN BATTERY CO.,LTD, has been selected for the simulation. The data provided by the manufacturer are given in the Tab.2.3.
In order to reach the desired voltage, 15 series-connected cells are needed.
Since the discharge voltage curve is not provided by the manufacturer, the eq.2.10 was adopted for the model of the battery, as shown in Fig.2.4. This approximation won't affect the analysis since the LiFePo4 battery is characterized by a quite flat V_{oc}-SOC curve, especially in the safety range of operation where it will be called to operate, which is for SOC maintained between 40 and 95 %.

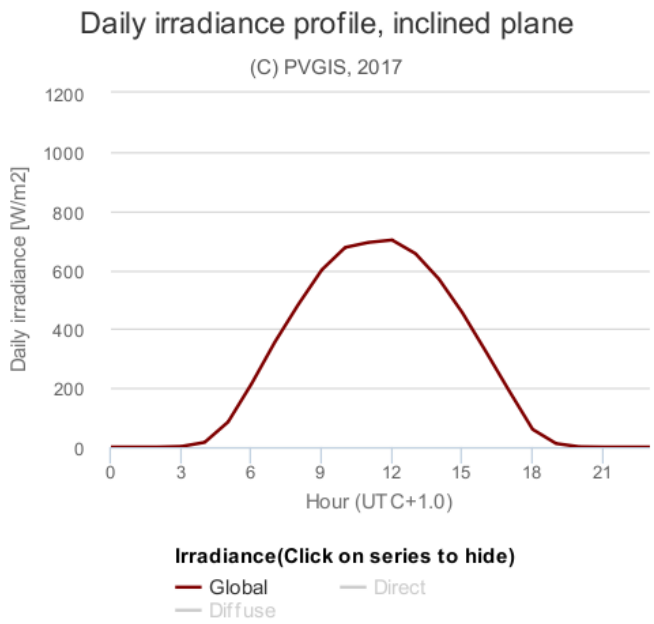

Figure 2.5: Daily average irradiance in June in Aalborg.

Data	**Value**
Nominal Voltage (V_n)	3.2 V
Charging Cut-off Voltage (V_{max})	3.65 V
Discharging Cut-off Voltage (V_{min})	2.5 V
Standard charging/discharging current (I_n)	$\frac{1}{3}C_3A$ (6.6 A)
Max continuous charging/discharging current (I_{max})	$3C_3$A (60.0 A)
Internal resistance (R_{int})	<2 mΩ

Table 2.3: Parameters of the battery cell.

2.4 Boost Converter Interfacing the PV

The interface between every PV module and its respective dc-link is realized by means of a dc-dc boost converter, which is shown in Fig.2.6. This is an unidirectional converter that enables the power transfer from the PV generator to the dc-link. Its main role is to ensure that the PV operation point is the one that maximize the extraction of power, known as the “maximum power point” (MPP). As shown in Fig.2.2, the typical power-voltage characteristic has a single maximum point (P_{mpp}, V_{mpp}), characterized by the I_{mpp} current. For this reason, in order to reach the goal, it is sufficient to enforced the PV voltage to be equal to the MPP voltage V_{mpp}.
The P-V and I-V curves are plotted for a particular condition of irradiance and temperature, but it is well known that during the day the external conditions change. As a consequence, the characteristic curves change during the PV operation.
The variability of the MPP can be smooth according to the typical daily irradiation profile, or sharp due to a quick change in the weather condition or for a temporary partial shading caused by an external factor, such as a bird or a cloud.
In order to dynamically track the MPP, the value of the voltage in which the PV should operate must be evaluated by a MPPT algorithm, independently performed by each PV module. However, before the developing of the control logic, it’s impor-

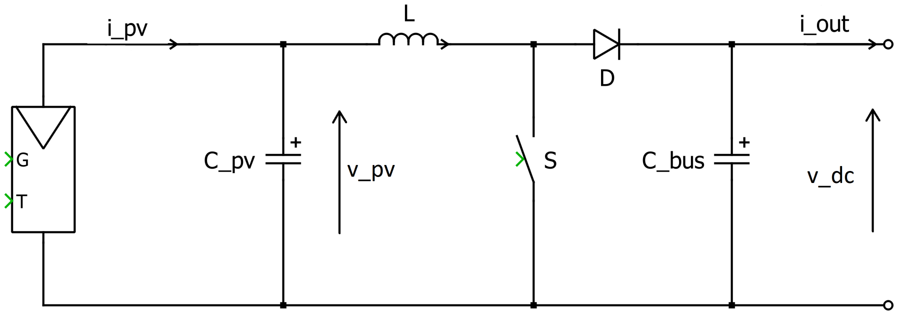

Figure 2.6: Dc-dc boost converter.

tant to conduct the modelling of the boost converter.
It is worth to point out that, in this application, the boost converter is supposed to always operate in Continuous-Conduction Mode (CCM). This means that the inductance L and the switching frequency f_s have been chosen in such a way that the current in the inductor never goes to zero during one switching period.
There are two major parameters that must be properly designed for the good operation of the boost converter: the inductance and the switching frequency.
Conventionally the switching frequency f_s is set around dozens of kHZ.
Whereas, the value of the inductance must be fixed such that the converter always operates in CCM with a desired ripple amplitude of the inductor current waveform, Δi_L^*. The value of L that fulfills this requirement can be obtained by observing that in steady-state conditions the moving average of the inductor current over one switching period is constant. Geometrical observations based on this assumption lead to the Eq.2.12, used to properly size the inductor [16].

$$L = \frac{V_{pv} D}{2 f_s \Delta i_L^*} \tag{2.12}$$

The sizing has been made by considering the panel operating at the MPP under STC, a dc-link voltage of 50 V and a maximum acceptable current ripple equal to the 10 % of the average value of the current.
In the end, an inductance of 0.3 mH and a switching frequency of 20 kHz have been chosen for the simulation.
The focus is now moved on the modelling. By applying the Kirchhoff's laws to the circuit in fig.2.6, while taking into account that the state variables are represented by the inductor current and the dc-link voltage, the state space model is derived as follows:

When S is on:

$$\begin{cases} L\frac{di_L}{dt} = v_{pv} \\ C_{bus}\frac{dv_{dc}}{dt} = -i_{out} \end{cases} \tag{2.13}$$

Whereas, when S is off:

$$\begin{cases} L\frac{di_L}{dt} = v_{pv} - v_{dc} \\ C_{bus}\frac{dv_{dc}}{dt} = i_L - i_{out} \end{cases} \tag{2.14}$$

Unfortunately, the model is time-variant, since the circuit configuration depends on the state of the switching device S and, therefore, the circuit averaging technique will be adopted [16].

Firstly, the switch network of the power converter is replaced with voltage and current sources, in order to obtain a time-invariant circuit topology.
With this aim, the control variable u is introduced:

$$u = \begin{cases} 1, & 0 \leq t \leq t_{on} \\ 0, & t_{on} \leq t \leq T_s \end{cases} \tag{2.15}$$

The model can be written as follows:

$$\begin{cases} L\frac{di_L}{dt} = v_{pv} - v_{dc}(1-u) \\ C_{bus}\frac{dv_{dc}}{dt} = i_L(1-u) - i_{out} \end{cases} \tag{2.16}$$

Secondly, the converter waveforms are averaged over one switching period, in order to remove the switching harmonics. The basic assumption that must be made is that the natural time constants of the converter network are much longer than the switching period. For a well designed converter, the hypothesis of a small ripple in the inductor current and capacitor voltage waveforms is always verified. If the basic assumption is satisfied, the dynamics of the system is well defined by considering only the low frequency variations, obtained by applying the moving average operator to the model.
The average over the switching period $\mathrm{T_s}$ of a given time function $x(t)$ is defined as:

$$\bar{x}(t) = \frac{1}{T_s}\int_{t-T_s}^{t} x(\tau)d\tau \tag{2.17}$$

In particular, the moving average of the discontinuous control function u is known as *duty ratio*:

$$d = \frac{1}{T_s}\int_{t-T_s}^{t} u(\tau)d\tau = \frac{t_{on}}{T_s} \tag{2.18}$$

Finally, the averaged model of a boost converter is obtained:

$$\begin{cases} L\frac{d\bar{i}_L}{dt} = \bar{v}_{pv} - \bar{v}_{dc}(1-d) \\ C_{bus}\frac{d\bar{v}_{dc}}{dt} = \bar{i}_L(1-d) - \bar{i}_{out} \end{cases} \tag{2.19}$$

The equivalent circuit representing the averaged model is shown in Fig.2.7, where the switching network in Fig.2.6 has been replaced by two controlled waveform sources $\mathrm{v_{control}}$ and $\mathrm{i_{control}}$, defined as follows:

$$\begin{cases} \bar{v}_{control} = \bar{v}_{dc}(1-d) \\ \bar{i}_{control} = \bar{i}_L(1-d) \end{cases} \tag{2.20}$$

At this point, all the converter waveforms are varying continuously over time. However, the model is nonlinear since it involves the multiplication between time-varying quantities. Since the objective is to design a proper controller for the boost converter, it would be better to use a linear model, in order to take all the advantages provided by the control theory for linear systems, such as the Laplace transform.

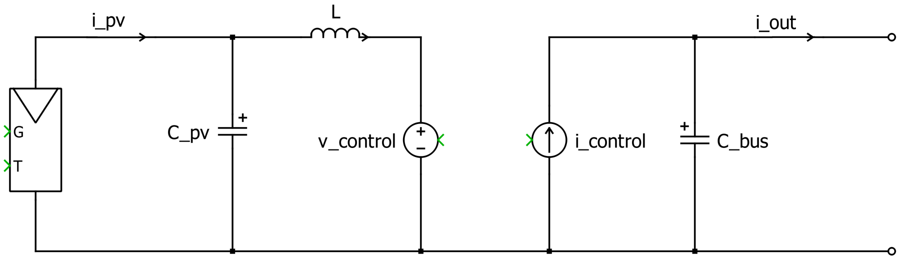

Figure 2.7: Dc-dc boost converter circuit averaged model.

In this regard, the linear small-signal model has been obtained by perturbing and linearizing the averaged model around a quiescent operating point.
Let's suppose that the converter has been driven in some steady state operation point:

$$\begin{cases} V_{pv} = V_{dc}(1-D) \\ I_{out} = I_L(1-D) \end{cases} \tag{2.21}$$

At this point, a small perturbation of the inputs is applied. Therefore, all the averaged waveforms can be defined as the sum of the steady state value and a small variation:

$$\begin{cases} \bar{v}_{dc} = V_{dc} + \hat{v}_{dc} \\ d = D + \hat{d} \\ \bar{i}_L = I_L + \hat{i}_L \\ \bar{i}_{out} = I_{out} + \hat{i}_{out} \\ \bar{v}_{pv} = V_{pv} + \hat{v}_{pv} \end{cases} \tag{2.22}$$

The latter are now substituted into the averaged model. Firstly, can be noticed that all the DC terms disappear, since they balance each other out, according to the steady-state equations. Furthermore, all the second order terms are neglected. This is a good approximation since they are much smaller in magnitude than the first order terms.
In the end, the following small signal model is yielded:

$$\begin{cases} L\frac{d\hat{i}_L}{dt} = \hat{v}_{pv} - \hat{v}_{dc}(1-D) + V_{dc}\hat{d} \\ C_{bus}\frac{d\hat{v}_{dc}}{dt} = \hat{i}_L(1-D) - I_L\hat{d} - \hat{i}_{out} \end{cases} \tag{2.23}$$

2.5 Half-Bridge Converter Interfacing the BESS

As mentioned above, two ways of physical connection are proposed for the battery module. As concerns the first topology, shown in Fig.1.6.(a), the battery is connected to the dc-link via a bidirectional dc-dc converter, shown in detail in Fig.2.8. It consists of a conventional half-bridge and an inductor placed on the battery port side. This architecture enables a bi-directional power flow, through the reversal of the current direction.

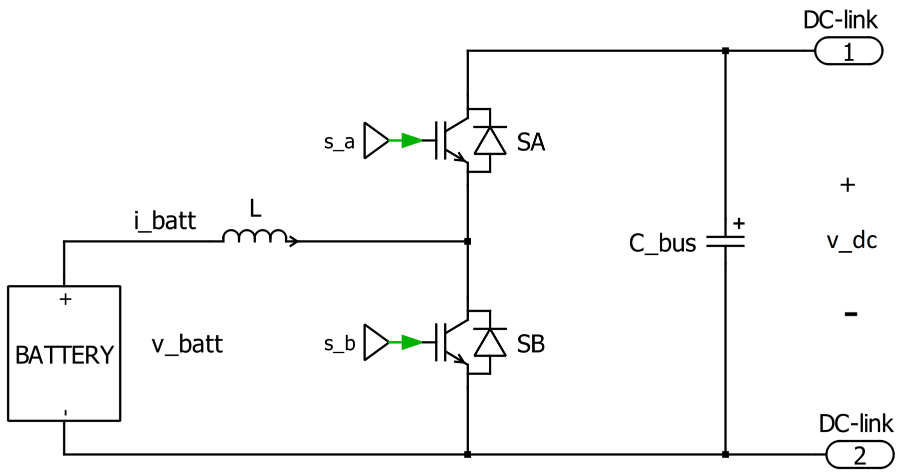

Figure 2.8: Bidirectional dc-dc converter.

The two switches are driven one at time, depending on whether the battery is charging or discharging.
During the discharging operation mode, the switch S_A is kept on off mode, while S_B is on switching mode. In this case, the power converter acts like a boost converter and the power flows from the battery towards the dc-link.
On the contrary, when the battery is charging, the switch S_A is switching, while S_B is kept on off mode. As a result, the power converter behaves like a buck converter whose input and output ports are represented by the dc-link and the battery terminals respectively.
The circuit network is once again time-variant, depending on the battery operation mode and on the state of the respective switching device.
In order to find a time-invariant model, exactly in the same way as was done for the PV boost converter, the following average model is built.

$$\begin{cases} L\frac{d\bar{i}_{batt}}{dt} = \bar{v}_{batt} - h\bar{v}_{dc} = \bar{v}_{batt} - \bar{v}_{control} \\ C_{bus}\frac{d\bar{v}_{dc}}{dt} = h\bar{i}_{batt} - \bar{i}_{out} = \bar{i}_{control} - \bar{i}_{out} \end{cases} \tag{2.24}$$

where the control variable h is defined as a function of the duty ratio of the two switching devices, d_A and d_B, according to the following statement:

$$h = \begin{cases} d_A, & charging \\ 1 - d_B & discharging \end{cases} \tag{2.25}$$

Finally, the switching network of the power converter can be replaced by the following controlled waveform sources, as can be seen in Fig.2.9.

$$\begin{cases} \bar{v}_{control} = h\bar{v}_{dc} \\ \bar{i}_{control} = h\bar{i}_{batt} \end{cases} \tag{2.26}$$

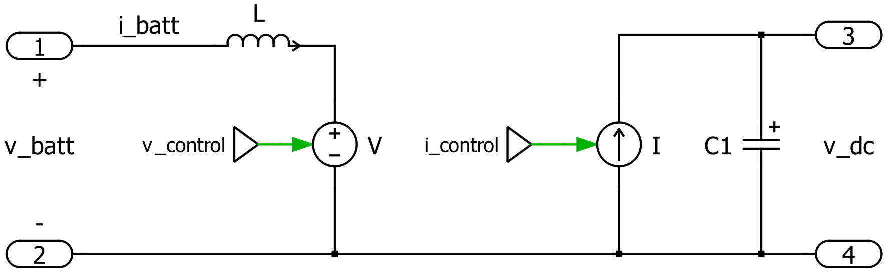

Figure 2.9: Bidirectional dc-dc converter averaged model.

Once more, with the view of taking advantages from the linear control techniques, the small signal model must be derived.
In the following, and in the subsequent controller design phase, the system is supposed to operate in boost mode. In order to highlight the state variables, a fictitious load is introduced, defined as:

$$R = \frac{V_{dc}^2}{P_{out}} \tag{2.27}$$

Therefore:

$$i_{out} = \frac{v_{dc}}{R} \tag{2.28}$$

Let's suppose that the converter has been driven in some steady state operation point:

$$\begin{cases} V_{batt} = V_{dc}(1-D) \\ I_{out} = I_{batt}(1-D) \end{cases} \tag{2.29}$$

By perturbing the system from this position and by neglecting all the second order terms, the small signal model is obtained:

$$\begin{cases} L\,\frac{d\hat{i}_{batt}}{dt} = \hat{v_{batt}} - (1-D_B)\,\hat{v}_{dc} + V_{dc}\,\hat{d_B} \\ C_{bus}\,\frac{d\hat{v}_{dc}}{dt} = (1-D)\,\hat{i}_{batt} - \frac{1}{R}\,\hat{v}_{dc} - I_{batt}\,\hat{d} \end{cases} \tag{2.30}$$

Chapter 3

Control Strategy

In this chapter the control strategy of the system is described and designed.

The CHB inverter consists of a certain number of power cells in series. Each cell is an active power generator, consisting of a PV module and a battery module. The major task of the system is to supply a desired active power to the grid. An high-level control will decide the state of each cell (i.e. inserted, by-passed, modulated) according to the deployed multilevel modulation strategy. However, since each power cell generator is independent, a local control must be developed and tested beforehand.
In the following, the low-level control strategy of a single power cell of the CHB inverter will be investigated. The subsystem can be seen as a three port network, where the power is exchanged between three subsystems: the PV generator, the battery energy storage system (BESS) and the output port, which represents the interface of a single full bridge sub-module.
In Fig.3.1 all the possible operation modes for a single sub-module are shown.

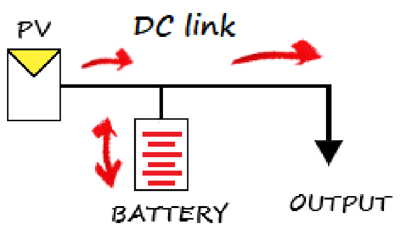

Figure 3.1: Operation modes.

It is important to point out that not all the ports enable a bi-directional power flow. More specifically, the power generated by the PV system is always injected into the dc-link, whereas the power at the output terminals is always absorbed. On the other hand, the rechargeable battery system enable a bi-directional power flow, depending on whether the battery is charging or discharging. That means that, as a general rule, the battery can be charged only by the PV generator.
But actually, when the PV is not producing, for example during the night hours, the power flow of the whole CHB inverter could be reversed in order to charge the batteries from the grid. However, this operation mode will not be considered in this work.
Two different topologies for the PV-BESS power cell have been proposed.
Hereafter, the topologies with and without the dc-dc battery converter, shown in Fig.3.2, will be referred as A and B respectively. As highlighted in fig.3.2, the main difference between them lies in the way in which the battery module is interfaced with the dc-link.

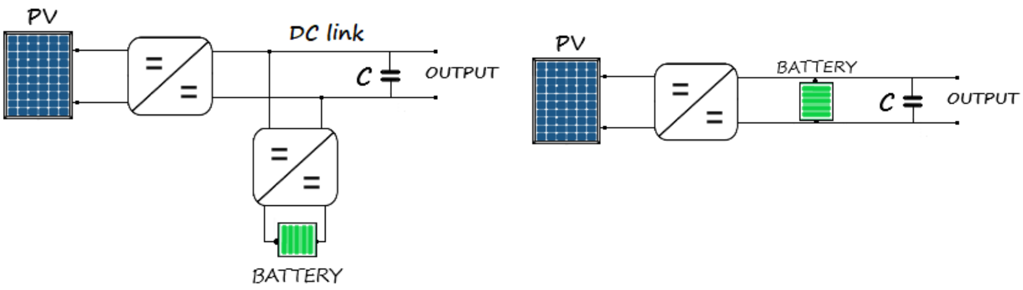

(a) (b)

Figure 3.2: Proposed power cell topologies.

In the first case, the battery is electrically decoupled from the dc-link capacitor by means of a bi-directional dc-dc power converter. In particular it consists of an half-bridge converter, which regulates the charging and the discharging processes of the battery by controlling the battery current.
Furthermore, it can also been used to control the voltage at the dc-link. In fact, the dc-link voltage can be subject to transient conditions, mainly resulting from power changes. These discrepancies from the reference can be compensated by properly charging or discharging the dc-link capacitor. The bi-directional battery converter suits best for this purpose, since it already requires a current control loop. However, when the battery is on the idle mode, the DC link voltage control must be managed by the grid converter, by increasing or decreasing the power injected into the grid, with respect to the power produced by the PV generator [17].
On the contrary, in the second topology, the battery is directly connected to the dc-link capacitor. In this case, the battery current, and thus also the battery power, can't be regulated as desired, but it automatically varies according to the unbalance between the load and the generation. As a result, the dc-link voltage can't be directly regulated, since it is affected by the SOC of the battery and by the charging or discharging battery current.
As far as concerns the interface between the PV module and the dc-link, in both cases a dc-dc boost converter is exploited. The latter has the main task of maximizing the power extraction from the PV module.
The control which drives the boost converter must be designed in order that the voltage at the PV terminals follows the MPP voltage, set as reference. For this purpose, an MPPT algorithm must be implemented.
In the following, the PV voltage and the battery current control loops are explained in detail.

3.1 MPPT Control

As mentioned above, in both cases of study, the dc-dc boost converter interfacing the PV module with the dc-link must be driven in such way that the voltage at the PV terminals is equal to the MPP voltage, even under varying weather conditions. With this purpose, a feedback control loop must be implemented. The PV voltage should follow the desired reference provided by the MPPT algorithm, that is continuously updated according to the external conditions. Furthermore, the stability and the transient behaviour of the feedback control loop must be taken into account

during the design phase. In order to evaluate the PV voltage reference that maximizes the extraction of solar power, a classic Perturb and Observe (P&O) MPPT algorithm has been implemented.
The operating principle of the P&O MPPT algorithm is outlined in the flowchart shown in Fig.3.3 [12].

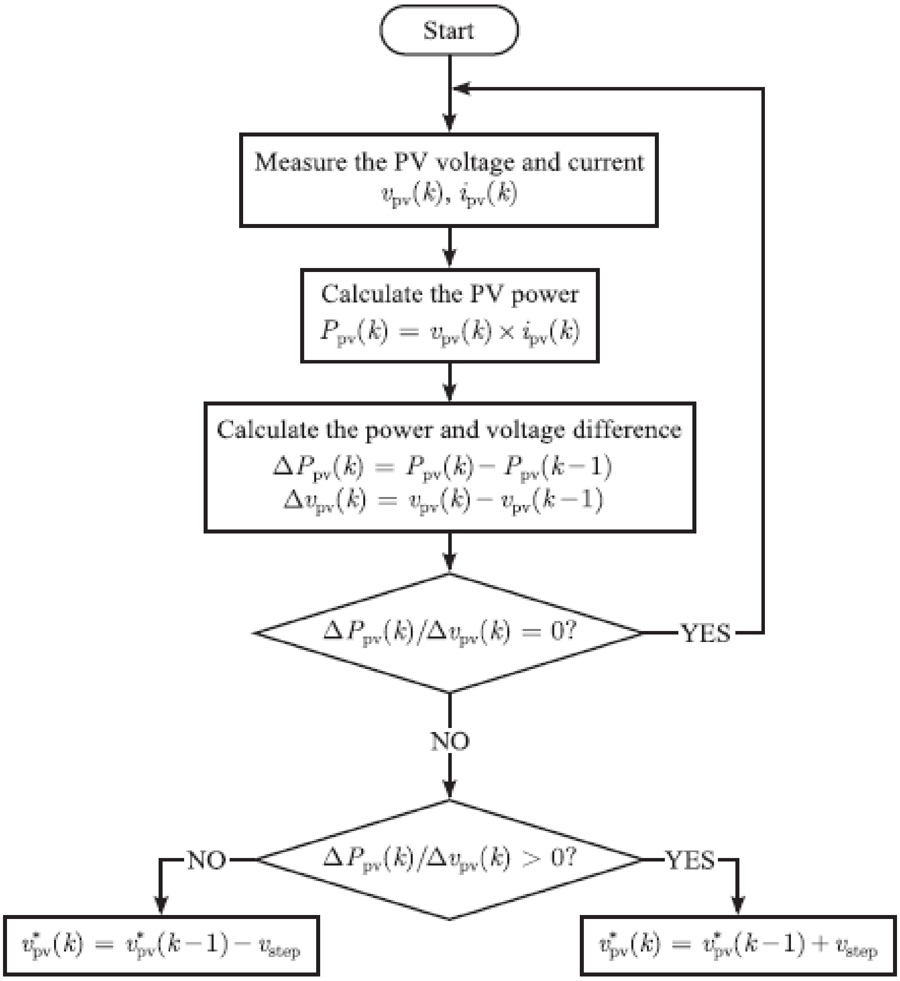

Figure 3.3: Flowchart of the Perturb and Observe MPPT algorithm [12].

The P&O algorithm is based on the fact that the P-V characteristic has only one maximum point.
According to the flowchart, every time period T_{MPPT} the operating voltage of the PV is perturbed in one direction and the resulting change in the power value is observed.
In response to a given perturbation, if the power rises, the next voltage perturbation will be given in the same direction. Conversely, if the power decreases, the direction of the next voltage perturbation will be reversed.
The voltage reference signal provided by the algorithm can be expressed as follows:

$$v^*_{pv}(k) = v^*_{pv}(k-1) + sgn\left(\frac{P_{pv}(k) - P_{pv}(k-1)}{v_{pv}(k) - v_{pv}(k-1)}\right) v_{step} \tag{3.1}$$

where k is the time step index.
In steady state conditions, the operating point of the P&O MPPT algorithm indefinitely oscillates around the MPP, in a range of $\pm$ v_{step}.

The performance of the MPPT algorithm depends on the perturbation frequency and on the voltage perturbation step size.
The higher is the voltage perturbation step size, the lower is the MPPT efficiency. In fact, a large voltage perturbation step results in a wider power oscillation during steady-state conditions, and thus in a lower average extracted power. On the other hand, during fast changes in the external conditions, a large step size speeds up the tracking of the MPP.
The choice of the perturbation step size involves a trade-off between the MPPT speed and efficiency.
As regards the choice of the MPPT algorithm frequency, it is necessary to consider that the system must reach the steady-state operation before applying the next perturbation.
In Fig.3.4 the feedback control loop for the dc-dc boost converter is shown.
The main role of the controller is to find the proper duty ratio in order to drive

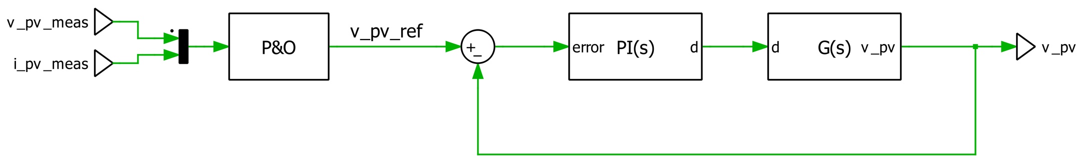

Figure 3.4: MPPT feedback control loop.

the boost converter in such way that the panel always operates at its MPP.
For the design of the controller, the dc-link voltage is supposed to be constant. The control variable is the duty ratio, while the output variable of interest is the voltage at the PV module terminals.
During the normal operation, for a well-designed controller, the system operates at its MPP. Hence, it is reasonable to consider the small signal model resulting from the linearization process around the MPP.
It is well known that the I-V characteristic of the panel is non linear. By defining the incremental conductance g, as shown in Eq.3.2, the linearized I-V relationship around the MPP is obtained, as highlighted in Eq.3.3.

$$g = -\left.\frac{di}{dv}\right|_{MPP} \tag{3.2}$$

$$\hat{i}_{pv} = -g\hat{v}_{pv} \tag{3.3}$$

By substituting the latter equation into the first equation of the small signal model, given in Eq.2.23, the equation which describes the dynamics of the PV voltage as a function of the duty ratio is yielded:

$$-gL\frac{d\hat{v}_{pv}}{dt} = \hat{v}_{pv} - \hat{v}_{dc}(1-D) + V_{dc}\hat{d} \tag{3.4}$$

The latter equation is linear and the control-to-output transfer function can be easily obtained by means of the Laplace transform. To achieve this, the input voltage variations $\hat{v}_{dc}$ is set to zero. Finally, the transfer function of the process is obtained:

$$G(s) = \left.\frac{\hat{v}_{pv}}{\hat{d}}\right|_{\hat{v}_{dc}=0} = -\frac{V_{dc}}{1+sgL} \tag{3.5}$$

The tuning of the PI controller can be conducted on MATLAB® in order to obtain a step response with a desired settling time and a stable feedback loop.
In the following, the PV voltage control loop will be tuned and tested.
As a general rule, the voltage perturbation step size is set around 1 % of the MPP voltage at STC. According to the data sheet of the PV module, $V_{MPPT} = 37.6\,\text{V}$. As a consequence, the perturbation step size has been set at 0.3 V. Furthermore, a time period T_{MPPT} of 0.1 s has been chosen.
Therefore, the PI parameters have been set in such a way that the closed loop step response settling time is smaller than T_{MPPT}. This condition guarantees that the PV voltage always reaches the steady state condition before that the next voltage reference perturbation is applied.

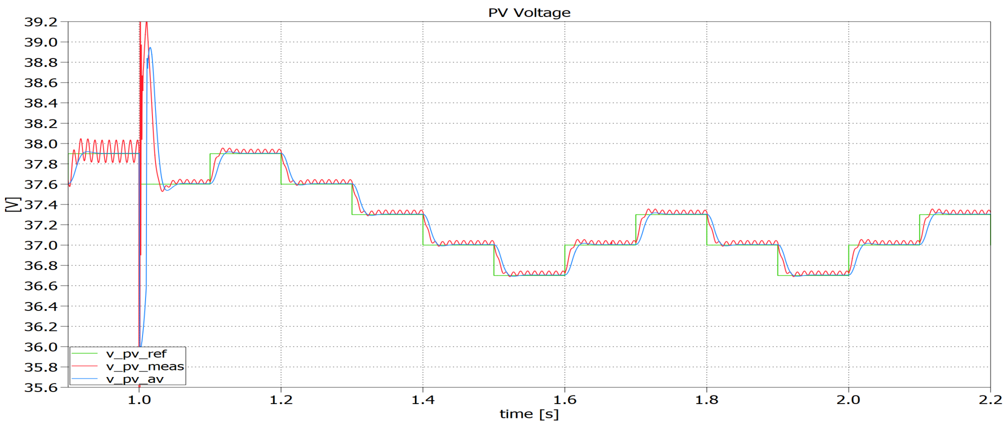

(a)

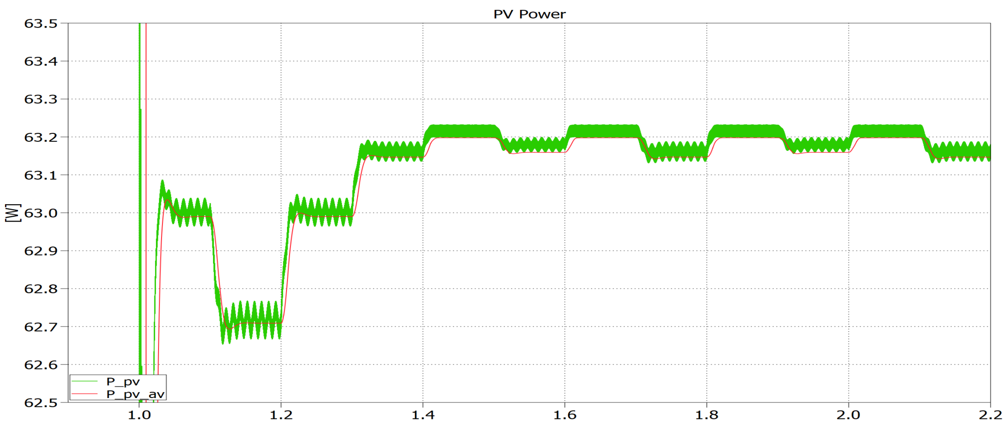

(b)

Figure 3.5: MPPT performance. (a) PV voltage and (b) PV power after a sudden change in the irradiation level in $t = 1\,\text{s}$.

With the purpose of verifying the performance of the control, a step change in the irradiation from $1000\,\frac{\text{W}}{\text{m}^2}$ to $200\,\frac{\text{W}}{\text{m}^2}$ is supposed to occur in $t = 1\,\text{s}$. The generated PV power instantaneously switches from around 331 W, provided under the previous STC, to around 60 W, due to an abrupt change in the photoelectric current.
This sharp change in the PV current results in a voltage overshoot. Hence, a small capacitor in parallel with the PV module is needed in order to avoid that the PV voltage is reversed.

Right after the abrupt operation point change, the system is not operating anymore at the MPP.
As highlighted in fig. 3.5 (a), the reference voltage is adjusted every T_{MPPT}, in order to track the new MPP. The fig. 3.5(b) shows that the power starts to increase, and after 4 $\mathrm{T_{MPPT}}$ periods, the system reaches the MPP. However, it can be noticed that the MPP won't be ever reached once and for all, but the PV power will keep on oscillating around it, even under steady-state conditions. This is a typical behaviour of the P&O algorithm.

3.2 Dc-link Voltage and Battery Current Control

In the first topology of study a bi-directional dc-dc converter is exploited to control the current in the battery, and thus the battery power. For this purpose, a current control loop should be implemented.
For the design of the half-bridge controller, the battery is supposed to operate within the allowed range of SOC values. With this assumption, it can both charge and discharge.
The bi-directional battery power converter has two main tasks.
Firstly, it has to provide the amount of power needed to compensate the unbalance between the PV production and the desired output power. Secondly, it must handle the regulation of the dc-link voltage, which is affected by power changes which may occur at any of the ports.

By giving a closer look at the scheme in fig.3.6, where the battery control loop is shown, it can be noticed that the control consists of two cascaded loops: an outer voltage loop, and an inner current control loop.
The inner control loop regulates the battery current, by means of a PI controller. The current reference is obtained by the sum of two components. The first one is the one responsible to transfer the active power needed to compensate the unbalance between the active power required by the load and the power produced by the PV. The second component is provided by the outer control loop which regulates the DC-link voltage.
This loop must be much slower than the inner current loop. This condition enable to decouple the dynamics of the two loops. In fact, during the design phase for the DC-voltage PI controller, it is possible to assume that the inner current loop operates instantaneously.

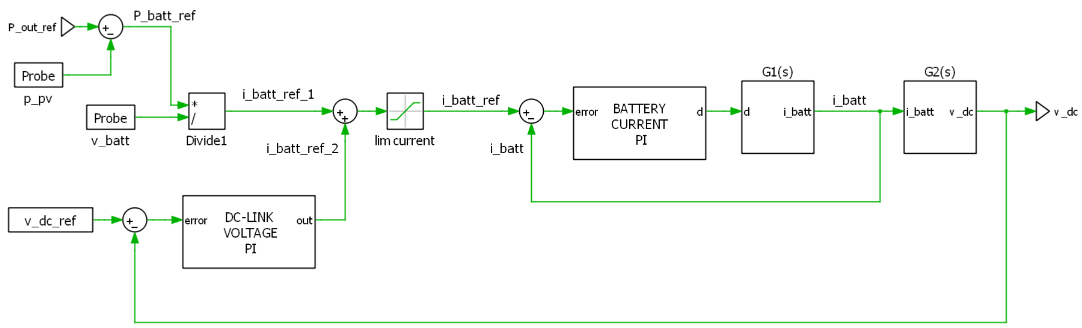

Figure 3.6: DC voltage and battery current loop.

In order to design the current and voltage PI controllers, the transfer functions, which define the relationship between the control variable and the battery current, and between the battery current and the dc-link voltage, are required.
Firstly, the control-to-battery current transfer function, has been derived from an easy manipulation of the half-bridge small signal model, given by the Eq.2.30. It should be recalled that the model has been obtained by assuming that the battery is discharging.
The small signal model of the boost converter can be written in a matrix form, by neglecting the small variation of the battery voltage, as follows:

$$\frac{d}{dt}\begin{bmatrix}\hat{i}_{batt}\\ \hat{v}_{dc}\end{bmatrix} = \begin{bmatrix}0 & \frac{-(1-D)}{L}\\ \frac{1-D}{C_{bus}} & \frac{-1}{RC}\end{bmatrix}\begin{bmatrix}\hat{i}_{batt}\\ \hat{v}_{dc}\end{bmatrix} + \begin{bmatrix}\frac{-V_{dc}}{L}\\ \frac{-I_{batt}}{C}\end{bmatrix}\hat{d} \tag{3.6}$$

This latter can be rewritten in a compact form, as follows:

$$\frac{d}{dt}\hat{\mathbf{x}} = A\,\hat{\mathbf{x}} + B\,\hat{d} \tag{3.7}$$

where $\boldsymbol{x}$ is the state variable vector and d is the control variable.
It is now easy to obtain the transfer function which binds the control variable with the state variables. In fact, by applying the Laplace transform to the Eq.3.7, it gets:

$$\frac{\hat{\mathbf{x}}}{\hat{d}} = (s\,I - A)^{-1}\,B \tag{3.8}$$

where s is the Laplace variable and I is the identity matrix.
From the latter matrix equation, the transfer function between the control variable and the battery current is obtained:

$$G_1(s) = \frac{\hat{i}_{batt}}{\hat{d}} = \frac{V_{batt}(2 + RC\,s)}{(1-D)[RLC\,s^2 + L\,s + R(1-D)^2]} \tag{3.9}$$

Secondly, the transfer function between the battery current and the dc-link voltage can be obtained from considering the power exchange between the battery, the dc-link capacitor and the rest of the system:

$$i_{batt}v_{batt} = C_{bus}\frac{d}{dt}v_{dc} + i_{out}v_{dc} \tag{3.10}$$

The small signal approximation of this power balance leads to the desired relation, obtained by neglecting the small variations of the battery voltage and of the output current:

$$G_2(s) = \frac{\hat{v_{dc}}}{\hat{i_{batt}}} = \frac{V_{batt}}{I_{out} + C_{bus}V_{dc}\,s} \tag{3.11}$$

Finally, from the knowledge of the transfer functions characterizing the plant, the tuning of the PI controllers have been conducted on MATLAB®, in order to guarantee the stability of the control loop. In particular, during the tuning was considered that the dynamics of the current control loop must be slower than the dynamics of the switching devices, and that the dynamics of the voltage loop must be slower than the dynamics of the inner current loop.

Chapter 4

Simulation Results and Comparison

This chapter describes the criteria used to perform the numerical analysis of the two proposed topologies. Five different simulations have been carried out on PLECS® in order to test every possible operation mode of the system. Finally, a comparison between the two topologies has been made, by focusing on the state of the battery and the efficiency.

4.1 Test Conditions

In order to understand the operation of the system, some observations about the power transfer should be made beforehand. A general truth for both the proposed topologies is that, in steady state conditions, the active power balance at the dc-link node is:

$$P_{pv} + P_{batt} = P_{out} \tag{4.1}$$

It can be noticed that the power related to the dc-link capacitor does not take part in the power balance. This is due to the fact that, in both cases, the voltage across the bus capacitor can be assumed constant and thus, on average, the capacitor won't charge nor discharge.
However, instantaneously the current through the capacitor is not equal to zero, since any change in the generated or demanded power results in a dc-link voltage variation. As a result, the voltage at the dc-link will consist of a dc component and an unwanted ripple. For the topology A, shown in Fig.3.2(a), the dc component is represented by the reference of the dc-link voltage control loop, while for the topology B, shown in Fig.3.2(b), it depends on the state of the battery.
In this application, the main causes of the dc-link voltage ripple are represented by the changes in the PV generated power and by the sinusoidal component of the output power at twice the grid frequency, resulting from the dc-ac conversion stage. Furthermore, high frequency harmonics results from the switching process of the several power converters.
For what concerns the PV generated power, its value depends on the external conditions of irradiance and temperature and on the performance of the MPPT algorithm which has been used.
As has already been mentioned, even under steady state conditions of the external

parameters, the P&O algorithm is characterised by an oscillating behaviour around the maximum power point. The amplitude of the power oscillation depends on the voltage step size chosen. It's clear that this phenomenon leads to a change in the injected PV power every MPPT period, that will affect the power balance.
For what concerns the power extracted from the output terminals of the cell, it is important to highlight that, actually, it will be handled by the grid current control which drives the entire cascaded H-bridge architecture. However, in order to test the low-level control of a single cell, before the realization of the CHB control, the load has been modelled as a controlled current generator.
With the intention of running a realistic simulation, the output current has been shaped like the dc-side current of a traditional full bridge inverter [18].
It mainly consists of two components, as shown in Eq.4.2: a dc component, which is responsible for the active power transfer, and a sinusoidal component with a frequency of twice the grid frequency, resulting by the dc-ac power conversion stage.

$$i_o = I_o + I_o \sin(2\omega_0 t) \tag{4.2}$$

where the average current I_o is linked to the desired output active power ${P^*}_{out}$ as:

$$I_o = \frac{P*_{out}}{V_{dc}}$$

Hence, the instantaneous output power is given by:

$$p_{out}(t) = v_{dc}(t) * i_o(t) \tag{4.3}$$

In particular, its DC component, P_{out}, represents the active power delivered to the grid, which takes part in the power balance, shown in Eq.4.1.
On this basis, it is clear that the battery supplies or absorbs the amount of power needed to compensate the difference between the active power required by the output terminals and the power produced by the PV.
However, it is important to take measures in order to avoid deep charging or deep discharging scenarios that may lead the battery to be seriously damaged.
With this purpose the following logic has been implemented:

1. $SOC_{min} < SOC < SOC_{max}$

   The battery can compensate for any mismatch between the PV power and the desired load, since it is allowed to both charge and discharge.

2. $SOC \geq SOC_{max}$ and $P^*_{out} < P_{pv}$

   The battery SOC has reached the upper limit and, at the same time, the desired output power is lower than the PV generation. Since the battery can't be further charged, the power delivered need to be increased to the PV power level. Hence, it will be set: $P^*_{out} = P_{pv}$

3. $SOC \leq SOC_{min}$ and $P^*_{out} > P_{pv}$

   The battery SOC has reached the lower limit and, at the same time, the power demand is higher than the PV generation. Since the battery can't be further discharged, the power delivered must be curtailed to the PV generated power level. Hence, it will be set: $P^*_{out} = P_{pv}$

During the simulation the SOC has been set at 50 %. In this way the battery is allowed to both charge and discharge, according to the desired output power. The two topologies have been simulated under five different test conditions, each one representing a different operation mode, which are listed below.

1. The power flows from the PV to the output port. The PV module is supposed to operate at STC (i.e. $G = 1000\,\mathrm{W/m^2}$ and $T = 25\,^{\circ}\mathrm{C}$). In these conditions it produces its rated power. The output power reference is set equal to the PV power, in order to withdraw the whole PV generation.

2. The power flows from the PV to the battery. The PV module is operating at STC, while the output power reference it set to zero. These conditions represent the case in which the cell is by-passed and the whole generated power is used to charge the battery.

3. The power flows from the battery to the output port. The PV module is supposed to be completely shaded, and the rated power required from the load is provided by the battery.

4. The power flows from the PV and the battery towards the output port. The PV is supposed to be partially shaded. In particular, the external conditions are set at: $G = 200\,\mathrm{W/m^2}$ and $T = 25\,^{\circ}\mathrm{C}$. The reference of the power demand is equal to the PV rated power. As a result, the battery is discharging in order to compensate the mismatch.

5. The power flows from the PV towards the battery and the output port. The PV is supposed to operate at STC, but the reference of the power demand is set at a lower value. As a result, the battery is charging in order to save the surplus of generated power.

Since the main difference of the two topologies lies in the way the battery is placed, the most relevant electrical parameters to look at during the comparison are the battery current, the battery power and the state of charge. Furthermore, the efficiency is calculated in each case. For the calculation of the efficiency, the estimation of the global losses is needed. Before showing the results of the simulation, in the following paragraph the way in which the losses have been estimated is described in detail.

4.2 Calculation of Losses

Unfortunately, in real systems part of the power which takes part in the power transfer is dissipated by unwanted effects. The major losses which have been considered for the calculation of the efficiency are the ones due to the heating of the internal resistance of the battery and of the ESR of the dc-link capacitor, and the ones related to the semiconductor devices.
The power dissipated across the battery internal resistance can be estimated as:

$$P_{batt} = R_{int} \cdot i_{batt}^2 \tag{4.4}$$

In the same way, the power losses across the ESR of the dc-link capacitor are given by:

$$P_C = ESR \cdot i_C^2 \tag{4.5}$$

For what concerns the power losses across the semiconductor devices, a deeper discussion is needed. As it is well known, the hypothesis of ideal semiconductor devices implies that, during the on-state, the device is modelled as an ideal short circuit, whereas during the off-state it is seen as an ideal open circuit. Furthermore, the turn-on and turn-off transient periods are supposed to occur instantaneously. If these assumptions are made, the losses across the switching devices can be considered equal to zero. However, in order to analyse the actual behaviour of the device, these hypothesis can't be no longer applied. The losses related to the switching devices are classified in conduction losses and switching losses.
The conduction losses are caused by the heating of parasitic resistance components of the semiconductor device, when it operates during the on-state.
Conduction losses are usually calculated as the product of the device on-state current and the device on-state voltage [19].
In particular, the on-state voltage is a function of the device parameters:

$$v_{on} = V_f + R_{on} \cdot i_{on}$$

where V_f is the forward voltage and R_{on} is the on-state resistance.
However, the on-state resistance varies significantly with the junction temperature, and can be challenging to define. In order to take into account this dependence, PLECS® allows to specify the on-state voltage as a function of the device current and temperature:

$$v_{on} = f(i_{on}, T) \tag{4.6}$$

By knowing this relationship, the conduction losses can be easily obtained as follows:

$$P_{conduction} = v_{on}(i_{on}, T) \cdot i_{on} \tag{4.7}$$

On the other hand, the switching losses arise from the fact that the transitions from the on-state to the off-state and vice versa do not occur instantaneously. During the transient interval, both the current through and the voltage across the device are substantially larger than zero, which leads to large instantaneous power losses [19]. The graph in Fig.4.1 shows the typical IGBT current and voltage pattern during the turn-on and the turn-off transient periods and the resulting dissipated power during one switching period.

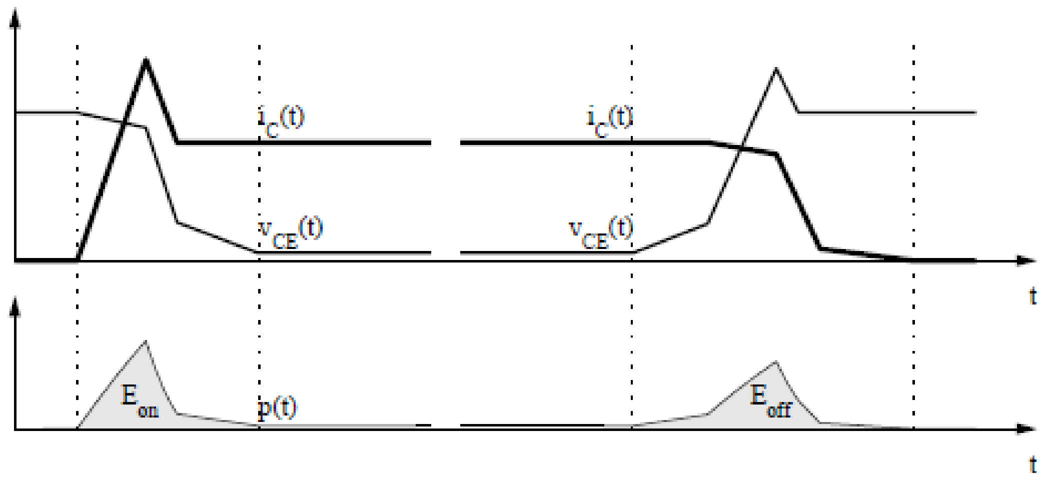

Figure 4.1: Turn-on and turn-off. On top: current and voltage; On bottom: switching losses [19].

PLECS® allows to specify the energy dissipated during the turn-on and the turn-off as a function of the on-state current i_{on}, of the off-state voltage v_{block}, and of the junction temperature T:

$$\begin{cases} E_{on} = g(v_{block}, i_{on}, T) \\ E_{off} = h(v_{block}, i_{on}, T) \end{cases} \tag{4.8}$$

From the knowledge of these relationships, the switching losses over one switching period T_s, are derived as:

$$P_{switching} = \frac{1}{T_s}[E_{on}(v_{block}, i_{on}, T) + E_{off}(v_{block}, i_{on}, T)] \tag{4.9}$$

Luckily, the relationships in Eq.4.6 and 4.8 are usually provided by the manufacturers, and can be easily implemented in the thermal editor of PLECS® in form of a look-up table.

On the basis of the global losses calculation, the efficiency of the system can be obtained as follows:

$$\eta = \frac{P_{pv} + P_{batt} - P_{losses}}{P_{pv} + P_{batt}} \times 100$$

4.3 Operation Mode 1: the PV Supplies the Output

The PV is supposed to operate at STC, producing an average power of 331.4 W, and the whole production is delivered to the output.

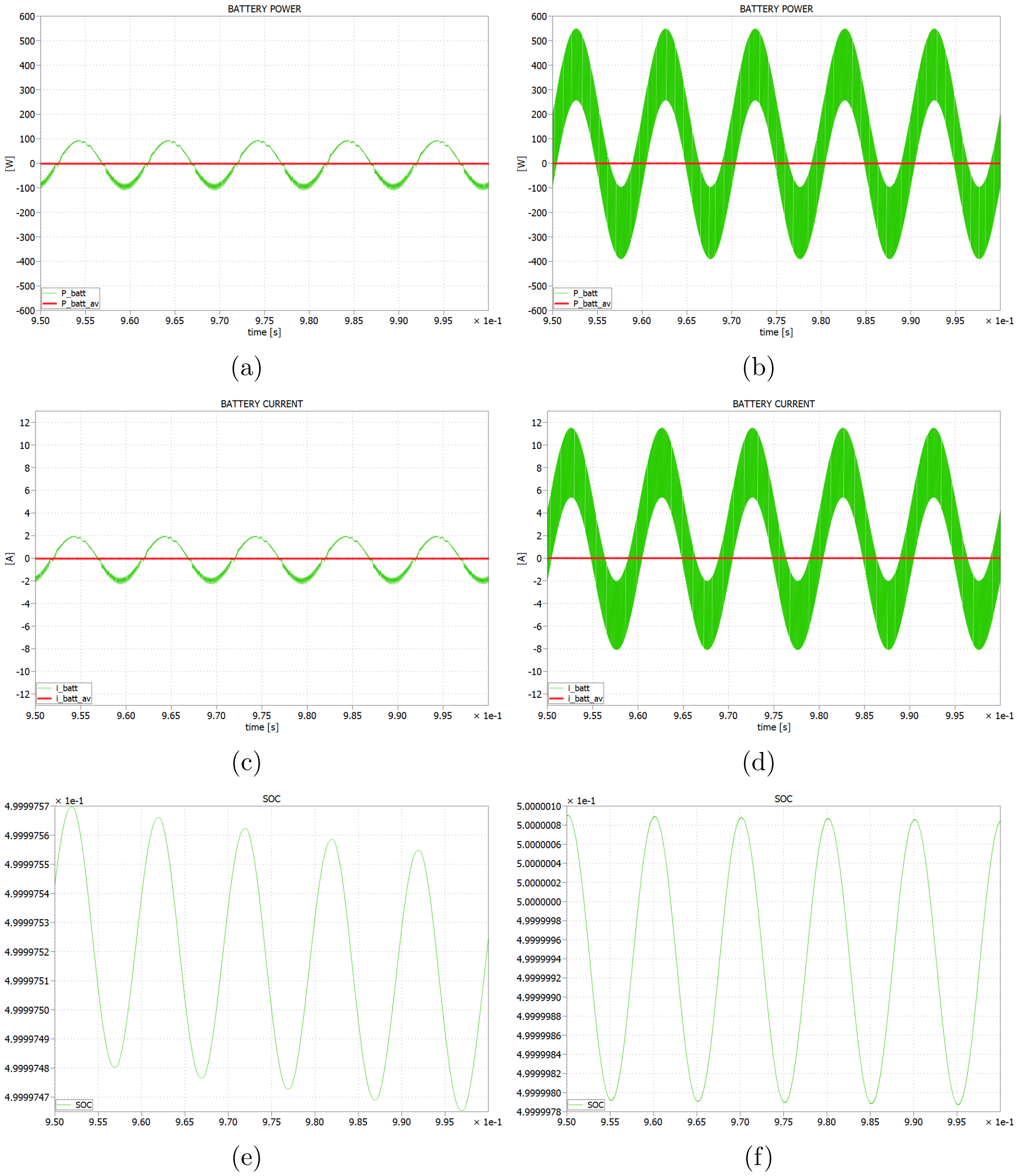

Figure 4.2: Battery power, current and SOC. sx: topology A; dx: topology B.

Topology	PV Converter Losses [W]	BESS Converter Losses [W]	Battery Ohmic Losses [W]	DC-link Capacitor Ohmic Losses [W]	Total Losses [W]	Efficiency [%]
A	12.8	1.4	0.06	2.1	16.4	95.1
B	12.7	/	0.9	0.1	13.7	95.9

Table 4.1: Losses.

4.4 Operation Mode 2: PV Supplies the Battery

The PV is supposed to operate at STC, producing 331.4 W, and the whole production is used to charge the battery.

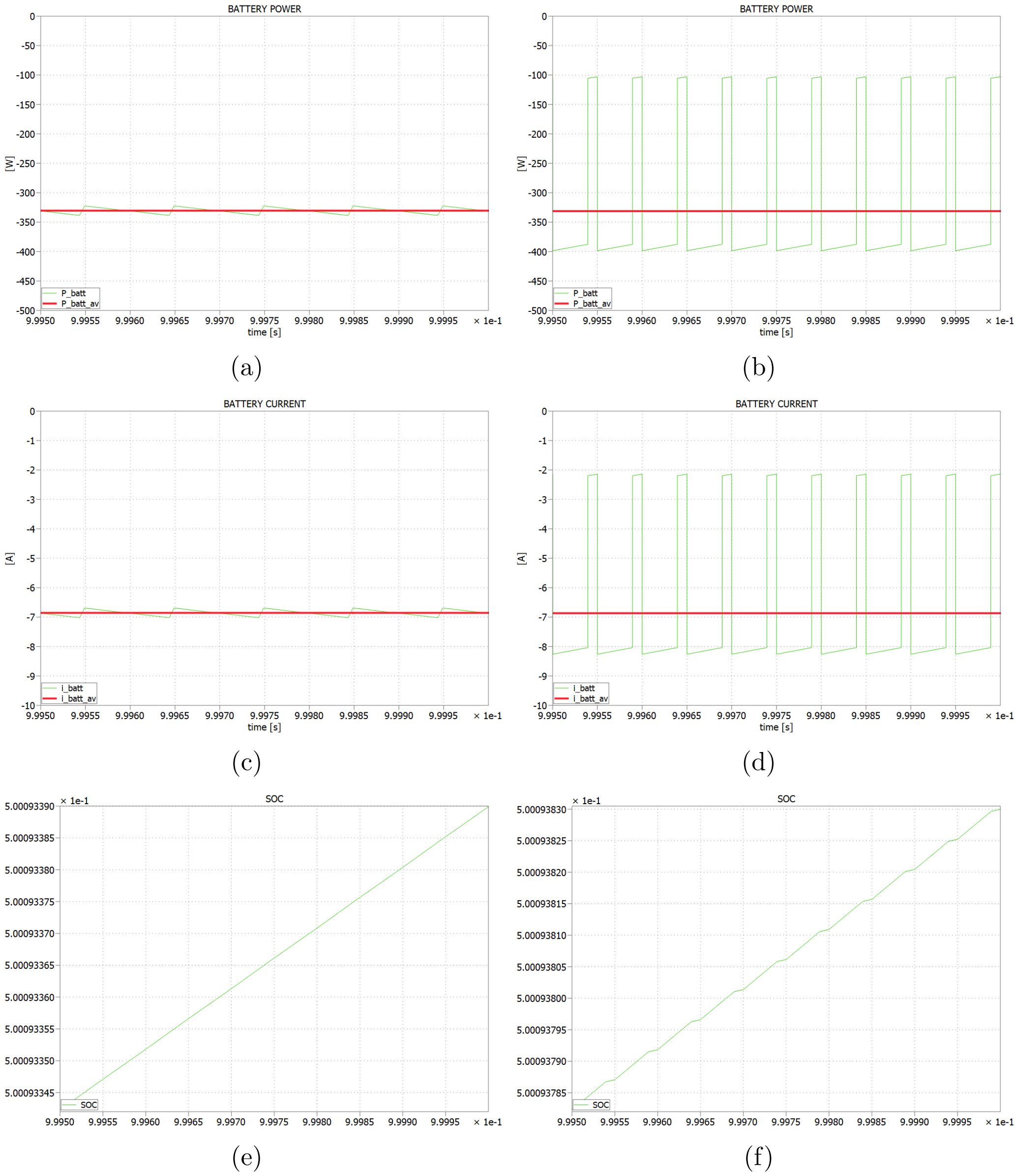

Figure 4.3: Battery power, current and SOC. sx: topology A; dx: topology B.

Topology	PV Converter Losses [W]	BESS Converter Losses [W]	Battery Ohmic Losses [W]	DC-link Capacitor Ohmic Losses [W]	Total Losses [W]	Efficiency [%]
A	12.8	9.3	1.4	0.8	24.3	92.7
B	12.7	/	1.6	0.1	14.4	95.7

Table 4.2: Losses.

4.5 Operation Mode 3: the Battery Supplies the Load

The PV panel is supposed to be completely shaded (i.e. $G = 0\,\frac{\mathrm{W}}{\mathrm{m}^2}$; $T = 25\,°\mathrm{C}$). The reference of the output power is set equal to the average power produced by the PV while it is operating at STC, i.e. 331.4 W. The battery will supply the full load demand.

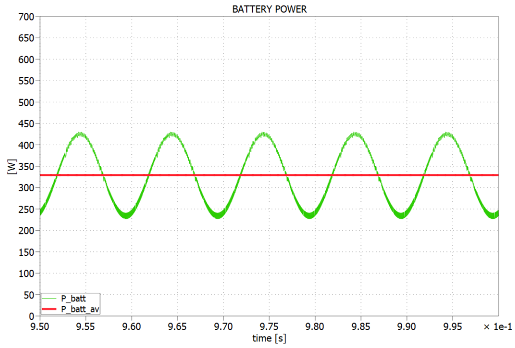

(a)

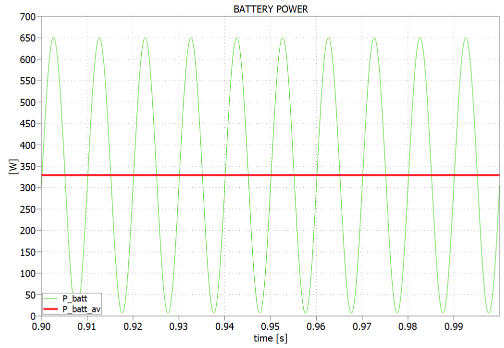

(b)

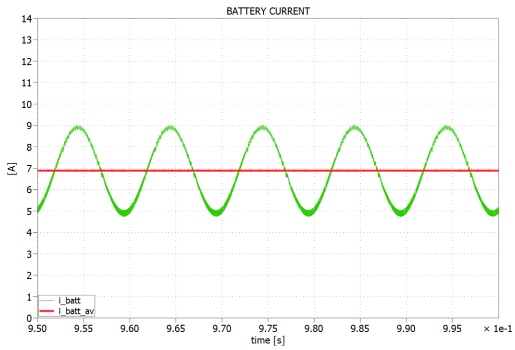

(c)

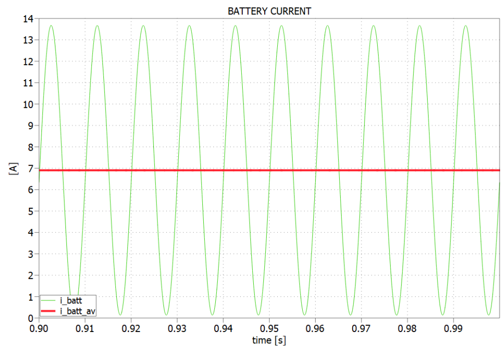

(d)

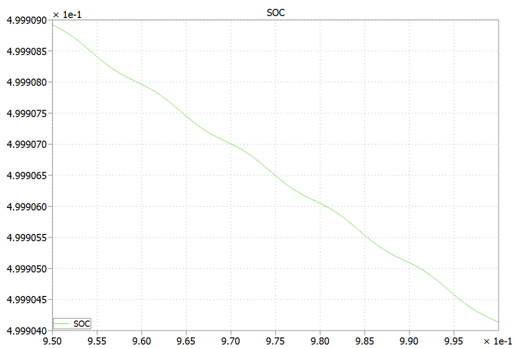

(e)

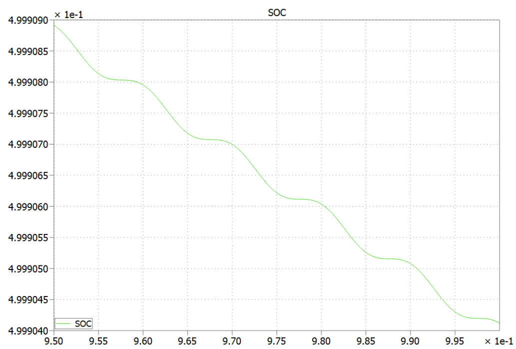

(f)

Figure 4.4: Battery power, current and SOC. sx: topology A; dx: topology B.

Topology	PV Converter Losses [W]	BESS Converter Losses [W]	Battery Ohmic Losses [W]	DC-link Capacitor Ohmic Losses [W]	Total Losses [W]	Efficiency [%]
A	0	9.3	1.5	1.4	12.2	96.3
B	0	/	2.1	0.01	2.1	99.4

Table 4.3: Losses.

4.6 Operation Mode 4: the PV and the BESS Supply the Load

The PV panel is partially shaded and it produces 65 W. The required output power is set equal to 331.4 W. The battery shall provide 266.4 W, needed to compensate the demand.

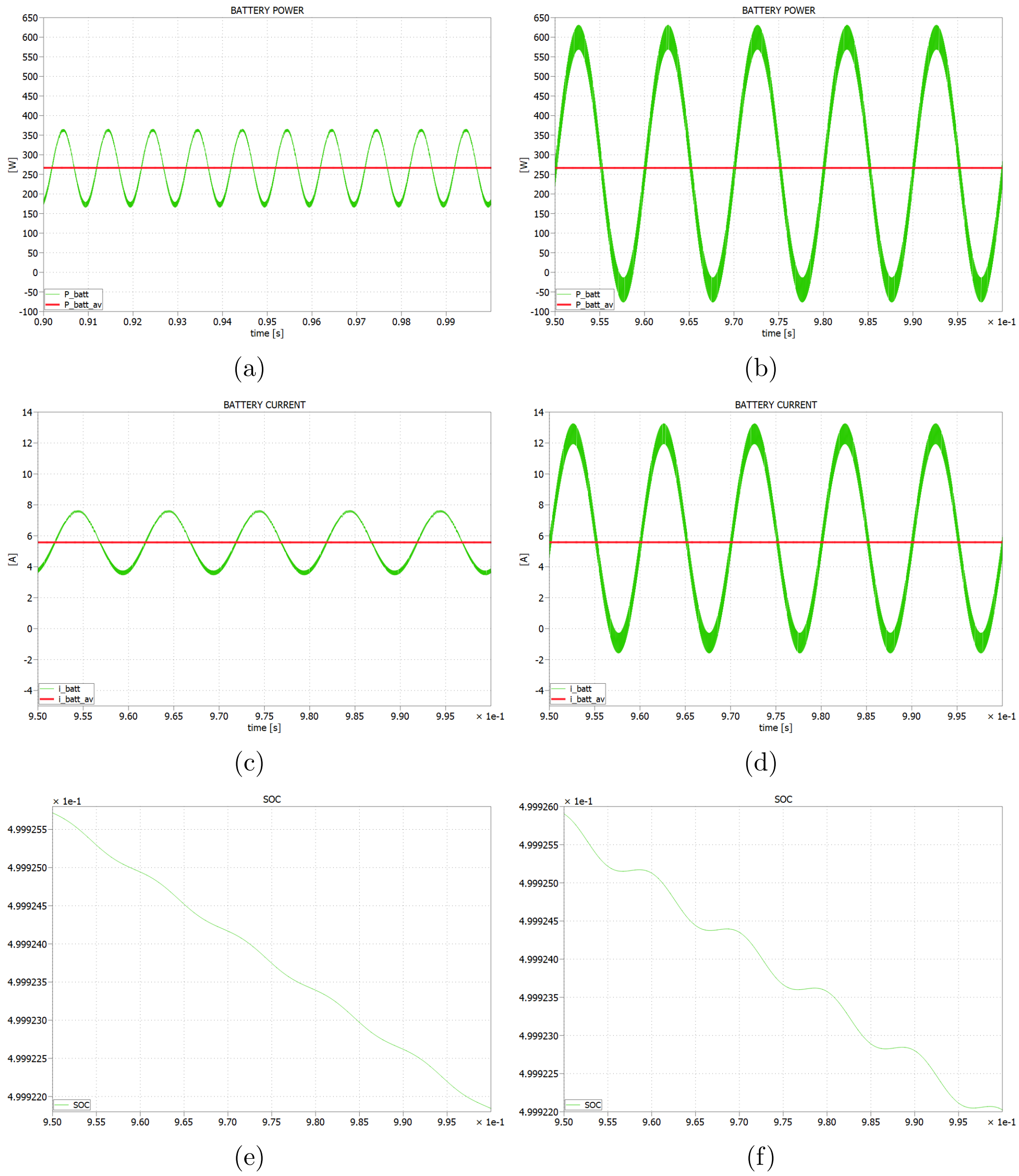

Figure 4.5: Battery power, current and SOC. sx: topology A; dx: topology B.

Topology	PV Converter Losses [W]	BESS Converter Losses [W]	Battery Ohmic Losses [W]	DC-link Capacitor Ohmic Losses [W]	Total Losses [W]	Efficiency [%]
A	2.0	7.3	1.0	1.3	11.6	96.5
B	2.0	/	1.6	0.01	3.6	98.9

Table 4.4: Losses.

4.7 Operation Mode 5: the PV Supplies the BESS and the Load

The PV panel is supposed to operate at STC, but the required output power is set at 150 W. The battery will charge in order to absorb the extra power produced by the panel, equal to 181.4 W.

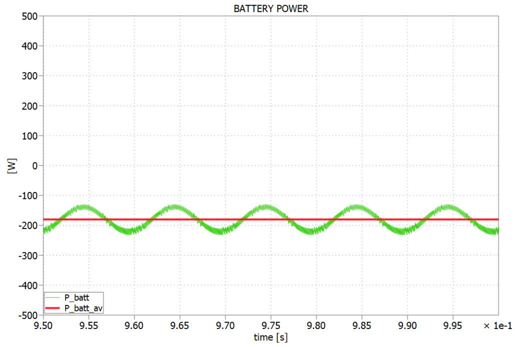

(a)

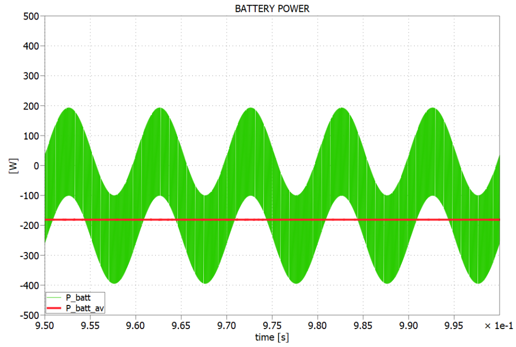

(b)

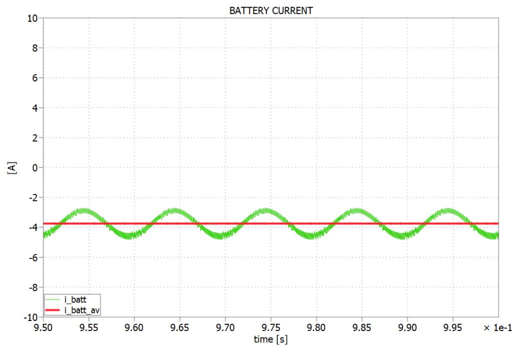

(c)

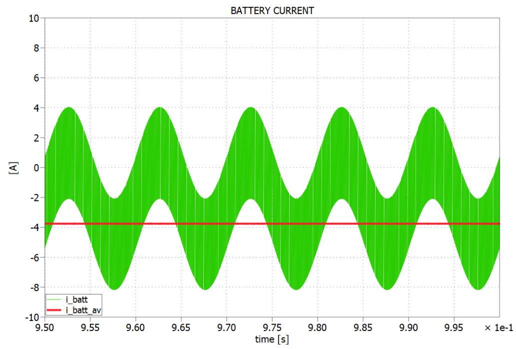

(d)

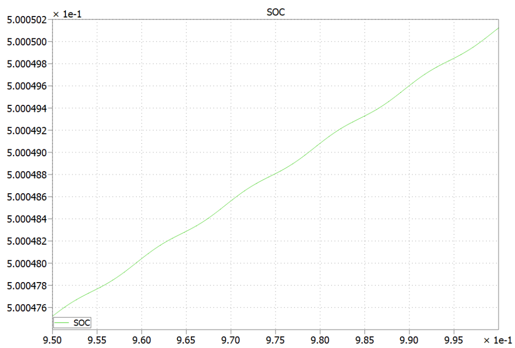

(e)

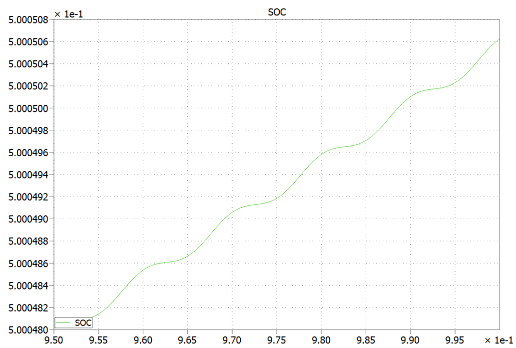

(f)

Figure 4.6: Battery power, current and SOC. sx: topology A; dx: topology B.

Topology	PV Converter Losses [W]	BESS Converter Losses [W]	Battery Ohmic Losses [W]	DC-link Capacitor Ohmic Losses [W]	Total Losses [W]	Efficiency [%]
A	12.8	4.4	0.4	1.1	18.7	94.4
B	12.7	/	0.8	0.1	13.6	95.9

Table 4.5: Losses.

4.8 Comparisons

From a close reading of the data obtained from the simulation, it clearly appears that, in every case, the ripple in the battery current profile is wider when the battery is directly connected to the dc-link (topology B). This is the result of all the power variations involving the dc-link. In fact, since the dc-link voltage is kept quite constant by the presence of the battery, these power variations are reflected on the battery current, and thus also on the battery power and on the SOC. As a consequence of this phenomenon, higher losses are dissipated in the internal resistance of the battery, when it is placed as in the configuration B.
On the other hand, the exploitation of a dc-dc converter to decouple the BESS module from the dc-link, enable to control the battery current and thus to reduce the ripple. In this case, all the power variations involving the dc-link, will be absorbed by the dc-link capacitor. As a result, the losses in the ESR of the dc-link capacitor turn out to be always higher for the topology A. Furthermore, in the configuration A, additional losses are generated during the dc-dc power conversion stage. These latter are the ones which affect the global efficiency the most.
As regards the battery, the worst scenario is represented by the 3^{th} operation mode, when it is called to supply the whole power demand. In this case, the internal battery losses are equal to 2.1 W for the topology B, compared to 1.5 W for the topology A. Nevertheless, an additional power of 9.3 W is dissipated in the configuration A, due to the additional dc-dc conversion stage. As a result, the mismatch between the global efficiency of the two topologies is equal to 3 percentage points: the configuration B achieves an efficiency of 95.7 %, compared to the one of the configuration A, equal to 92.7 %.

4.8.1 Efficiency under different irradiance levels

It is important to notice that the value of the efficiency is strongly related to the power flowing through the power converter. However, in a solar system the production is closely related to the value of the irradiance that hits the PV surface, which is remarkably variable during the day.
By keeping this in mind, the most likely operation mode is now investigated: a desired amount of power is required to be injected into the grid, independently by the PV generation. The battery is supposed to be fully charge, such that it can compensate for the difference between the PV production and the desired load. Depending on the size of this mismatch, the efficiency of the system changes.

In order to investigate how the efficiency is affected by the amount of power required by the battery, six different simulations are carried out, by varying the external irradiance with a step of 200 W/m^2, from 1000 W/m^2 to 0 W/m^2. The reference of the output power is set equal to the rated power of the PV module, and it is kept fixed for all the cases. Hence, the total power required by the load is partitioned in different proportions between the PV and the BESS, for every case.
In Tab.4.6 the losses and the efficiency resulting from the simulations, for both the configurations A and B, are shown.
In Fig.4.7, the values of the efficiency of the two topologies are plotted as a function of the BESS power, expressed in relative values of the PV rated power.

Case	Topology	PV Converter Losses [W]	BESS Converter Losses [W]	Battery Ohmic Losses [W]	DC-link Capacitor Ohmic Losses [W]	Total Losses [W]	Efficiency [%]
$1000\,\mathrm{W/m^2}$	A	12.7	1.2	0.04	2.2	16.2	95.1
$p_{bess} = 0$	B	12.7	/	0.8	0.1	13.6	95.9
$800\,\mathrm{W/m^2}$	A	9.6	1.8	0.09	1.8	13.3	96.0
$p_{bess} = 0.2$	B	9.6	/	0.8	0.07	10.5	96.8
$600\,\mathrm{W/m^2}$	A	6.8	3.3	0.3	1.6	12.0	96.4
$p_{bess} = 0.4$	B	6.8	/	1.0	0.05	7.9	97.6
$400\,\mathrm{W/m^2}$	A	4.2	5.2	0.6	1.4	11.4	96.6
$p_{bess} = 0.6$	B	4.2	/	1.2	0.03	5.4	98.4
$200\,\mathrm{W/m^2}$	A	2	7.3	1.0	1.3	11.6	96.5
$p_{bess} = 0.8$	B	2	/	1.6	0.02	3.6	98.9
$0\,\mathrm{W/m^2}$	A	0	9.3	1.5	1.4	12.2	96.3
$p_{bess} = 1$	B	0	/	2.1	0.02	2.1	99.4

Table 4.6: Losses and efficiency under different irradiance level.
(topology A: BESS with dc-dc; topology B: BESS directly connected).

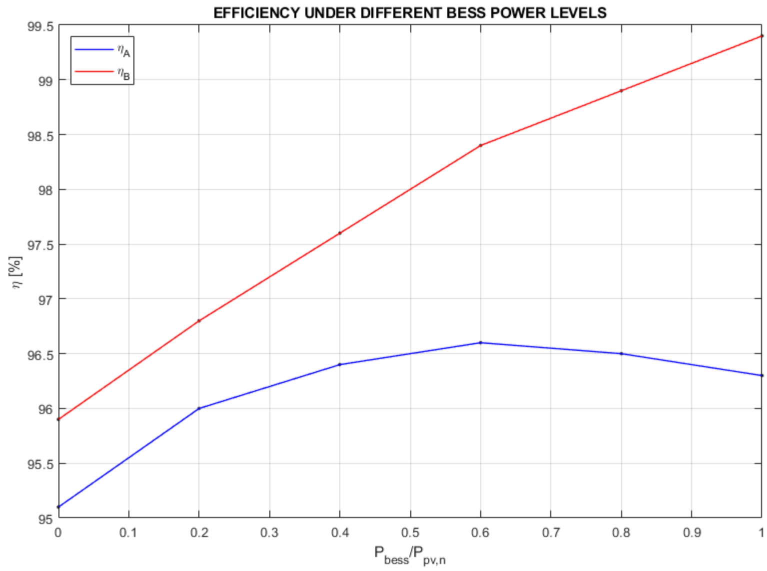

Figure 4.7: Efficiency of the two topologies under different power partitions.

By giving a closer look to the graph, it is clear that when the battery is directly connected to the dc-link the efficiency is always higher. However, the mismatch between the efficiency of the two configurations becomes relevant when the battery is called to provide an high amount of power. In this case, the additional dc-dc conversion stage leads to a marked increase of the losses.

4.8.2 European Efficiency

From the analysis of the different operating conditions, it emerged that the efficiency of the system depends on the power flowing through each power converter. Since the solar power varies during the hours of the day, a reasonable way to compare the efficiency of solar power converters is based on the European efficiency. The European efficiency takes into account the actual solar production over the entire day, by means of some weight coefficients. It is defined as shown in Eq.4.10, where the parameter $\eta_{i\%}$ represents the efficiency of the conversion system when operating at $i\%$ of its rated power.

$$\eta_{EU} = 0.03 \cdot \eta_{5\%} + 0.06 \cdot \eta_{10\%} + 0.13 \cdot \eta_{20\%} + 0.10 \cdot \eta_{30\%} + 0.48 \cdot \eta_{50\%} + 0.20 \cdot \eta_{100\%} \quad (4.10)$$

In order to calculate the European efficiency of the two hybrid PV-BESS systems, a typical daily operating condition is required to be fixed. For what concerns the PV daily production, the average daily profile of the month of June in Aalborg has been considered. As it is shown in Fig.4.8, the average irradiance over the daylight hours is equal to 338.4 W/m2.

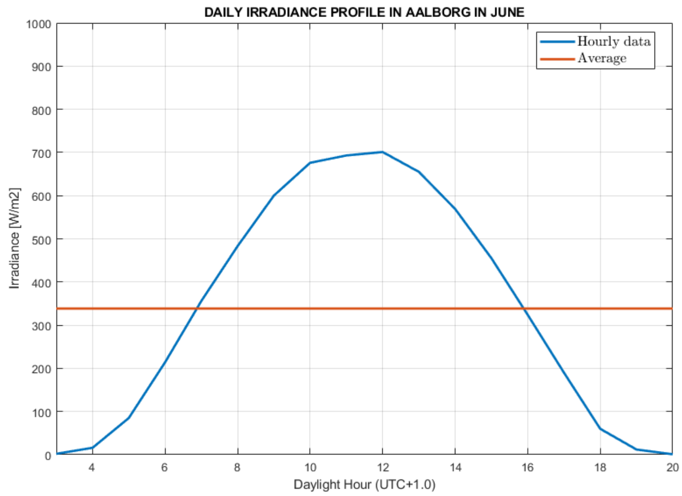

Figure 4.8: Irradiance daily profile typical of June in Aalborg.

For the calculation only the daylight hours have been taken into account, from 3 AM to 8 PM of the local time, because during the night the system is supposed to be out of operation. The reference of the output power has been set equal to the average daily production of the PV module used in the simulation, which is equal to 110.4 W.

Case	Topology	PV Converter Losses [W]	BESS Converter Losses [W]	Battery Ohmic Losses [W]	DC-link Capacitor Ohmic Losses [W]	Total Losses [W]	Efficiency [%]
50 W/m^2	A	0.5	2.4	0.1	0.2	3.2	97.1
$p_{pv} = 0.05$	B	0.5	/	0.2	0.002	0.7	99.4
100 W/m^2	A	1.0	2.0	0.09	0.2	3.3	97.0
$p_{pv} = 0.1$	B	1.0	/	0.2	0.003	1.2	98.9
200 W/m^2	A	2.0	1.2	0.03	0.2	3.4	96.9
$p_{pv} = 0.2$	B	2.0	/	0.1	0.005	2.1	98.1
300 W/m^2	A	3.1	0.6	0.006	0.2	3.9	96.5
$p_{pv} = 0.3$	B	3.1	/	0.09	0.01	3.2	97.1
500 W/m^2	A	5.4	1.3	0.04	0.4	7.1	93.6
$p_{pv} = 0.5$	B	5.4	/	0.2	0.02	5.6	94.9
1000 W/m^2	A	12.7	5.6	0.63	1.0	19.9	82.0
$p_{pv} = 1$	B	12.7	/	0.9	0.09	13.7	87.6

Table 4.7: Losses and efficiency under different irradiance level.
(topology A: BESS with dc-dc; topology B: BESS directly connected).

Under this operating condition, the battery SOC performs one cycle per day. In other words, during one day the battery is charging and discharging, by returning at the same initial value of SOC.
In order to calculate the European efficiency, six parameters $\eta_{i\%}$ are needed. For this purpose, six simulations have been performed by fixing different levels of irradiance,

each related to a different percentage of the PV rated power. For example, to calculate the parameter $\eta_{5\%}$, the PV production should be the $5\,\%$ of the PV rated power, and thus the irradiance has been set at $50\,\mathrm{W/m^2}$, which corresponds to the $5\,\%$ of its STC value.
In the table 4.7 the losses and the efficiency resulting from the performed simulation for the both PV-BESS configurations are shown.

At this point it is possible to compare the European efficiency of the two topologies. By applying the Eq.4.10, it results that the configuration which connects directly the BESS to the dc-link achieves an European efficiency higher by 2.2 percentage points with respect to the other.

$$\begin{cases} \eta_{EU,A} = 92.3\,\% \\ \eta_{EU,B} = 94.5\,\% \end{cases} \tag{4.11}$$

Chapter 5

Dc-ac stage: Cascaded H-Bridge Inverter

N different PV-BESS modules are now connected to a single-phase grid by means of a multilevel CHB inverter. Different control strategies should be implemented for the two proposed topologies. However, due to severe challenges in controlling the battery power without a dc-dc converter, only the topology which includes the additional dc-dc stage has been investigated in this chapter.

5.1 Modelling of the CHB Inverter

The CHB inverter consists of N series connected H-bridge sub-modules (SM). In Fig.5.1 the electric scheme of the single phase CHB is shown. Each H-bridge provides an output voltage $v_{h,i}$, which depends on the i-th dc-link voltage, according to value of the control variable h_i, as follows:

$$v_{h,i} = h_i \, v_{dc,i} \tag{5.1}$$

The control variable h_i can assume three possible values, according to the states of the switches of the i-th sub-module, as listed in the Tab.5.1.

$S_{A,i}^+$	$S_{A,i}^-$	$S_{B,i}^+$	$S_{B,i}^-$	h_i
on	off	on	off	0
off	on	off	on	0
on	off	off	on	+1
off	on	on	off	-1

Table 5.1: Switching states.

As a result, the output voltage waveform of the CHB can assume $2N + 1$ levels, and it is given by:

$$v_{inv} = \sum_{i=1}^{N} v_{h,i} \tag{5.2}$$

In the case of study, every SM capacitor is connected to an active power generator, consisting of a PV and of a BESS module. The i-th power cell injects the current

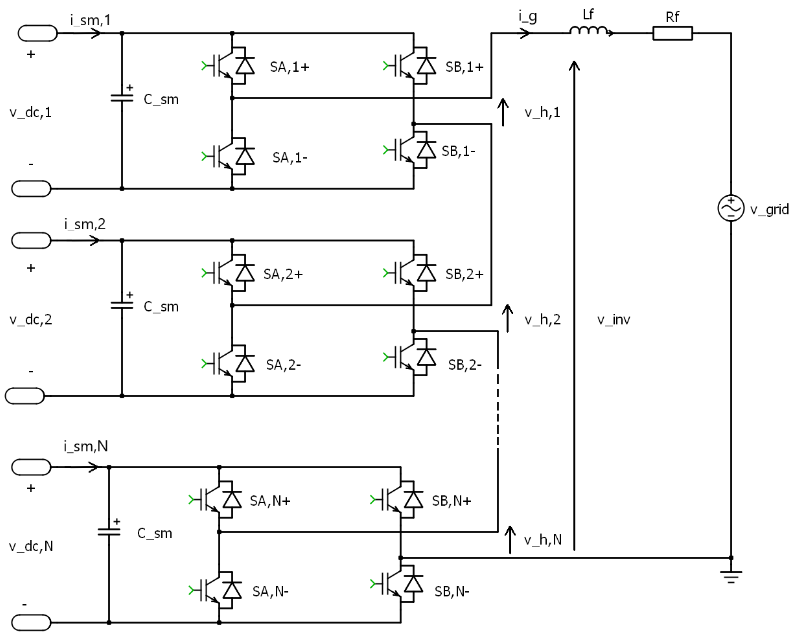

Figure 5.1: Single phase grid-connected Cascaded H-bridge.

$i_{SM,i}$ in the i-th dc-link. Meanwhile, on the ac-side, the PV-CHB multilevel system is connected the PCC of a single-phase low-voltage grid through an inductive filter, which has the main goal of suppressing the high frequency harmonic component resulting from the switching process.
By applying the Kirchhoff's laws to the circuit in Fig.5.1, the model of the system can be obtained, as described in the Eq.5.3.

$$\begin{cases} L_f \dfrac{d\, i_g}{dt} = \displaystyle\sum_{i=1}^{N} h_i\, v_{dc,i} - R_f\, i_g - v_g \\ C_{SM,i} \dfrac{d\, v_{dc,i}}{dt} = i_{SM,i} - h_i\, i_g \quad \forall \text{ i} = 1,\ldots,\text{N} \end{cases} \tag{5.3}$$

During the sizing phase of the system the following assumptions have been made:

- The overall dc-link voltage must be higher than grid voltage amplitude, in order to inject the active power from the PV modules into the grid. A margin of 20 % of the grid voltage peak value has been considered for the calculation of the overall dc-link voltage.

- The dc-link voltage of the single sub-module must be higher than the open circuit voltage of the PV module and of the BESS voltage in order to achieve a good operation of their power converters.

- The output filter inductance is typically sized as the 20 % of the base inductance of the system.

- The output filter resistance is typically sized as the 5 % of the base impedance of the system.

The parameters of the system are shown in Tab.5.2.

Parameters	Value
RMS Grid Voltage (V_g)	230 V
Grid Frequency (f_g)	50 Hz
Number of cells (N)	9
Maximum Power (S_n)	3.2 kVA
SM Dc-link Voltage reference ($V^*{}_{dc,SM}$)	50 V
Filter Inductance (L_f)	10 mH
Filter Resistance (R_f)	0.8 mΩ

Table 5.2: Parameters of the system.

5.2 Control Strategy

Every cell of the CHB inverter is connected to a PV-BESS active cell, as shown in Fig. 5.2. The PV module is interfaced with the SM by means of a boost converter, which performs the tracking of the MPPT according to the control strategy shown in Fig.3.4. Whereas, the BESS module is interfaced to the SM by means of a bidirectional dc-dc converter, which controls the battery power in order to compensate the mismatch between the power demand set-point and the PV production. The control strategy adopted is similar to the one shown in Fig.3.6; the only difference is that, here, the dc-link voltage loop has been removed. The dc-link voltages of all the SMs are now managed by the grid current control loop. For this reason, the control strategy consists of two control loops, as shown in Fig.5.3.

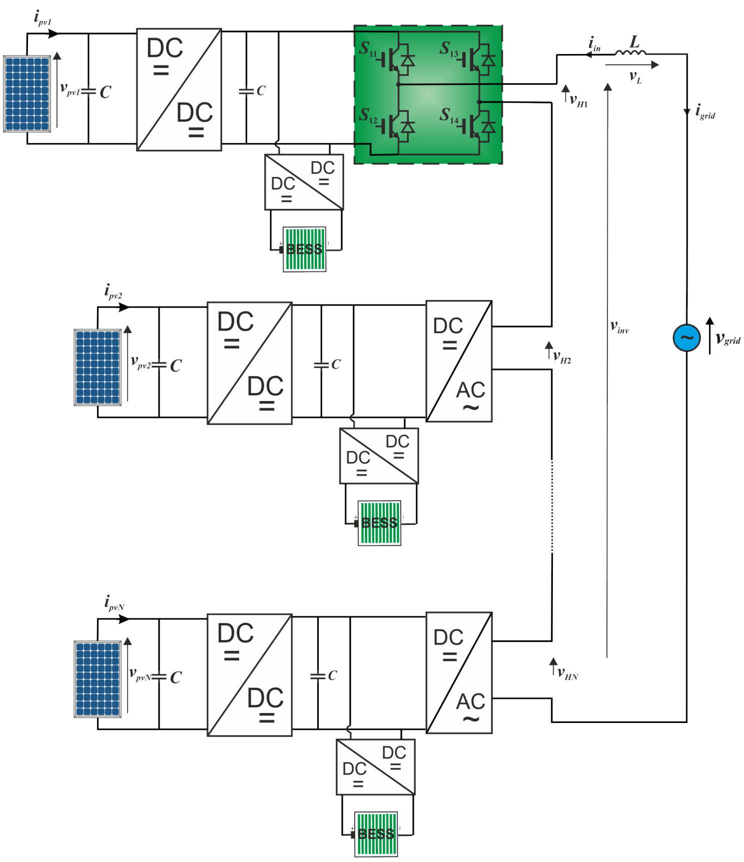

Figure 5.2: Circuit diagram of the single-phase CHB fed by PV-BESS cells.

The outer loop aims to control the dc-link voltages. It is based on the voltage-square control method [20].
A PI controller provides the value of active power needed in order to cancel the error between the average of the N dc-link voltages and the dc-link voltage reference, that is supposed to be the same for all the cells.

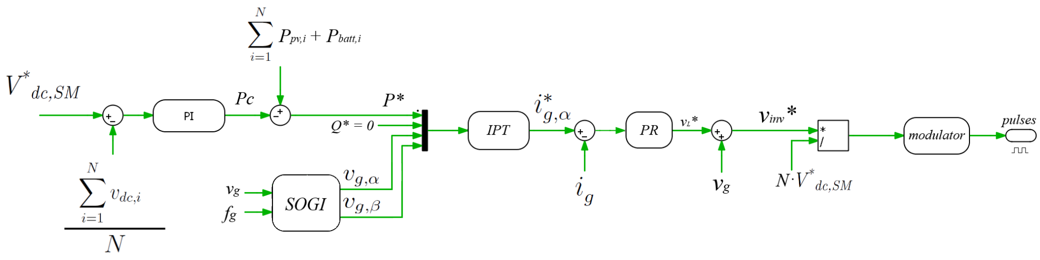

Figure 5.3: Grid current control strategy.

The inner control loop has the main task of controlling the grid current. The control strategy is based on the instantaneous power theory, which operates with voltages and currents expressed in the $\alpha\beta$ stationary reference frame.
According to the instantaneous power theory, the positive and negative-sequence of the grid current are functions of the desired instantaneous active and reactive power, referred to as p^* and q^* respectively. They are given by [17]:

$$\begin{bmatrix} i^*_{g,\alpha} \\ i^*_{g,\beta} \end{bmatrix} = \frac{1}{v^2_{g,\alpha} + v^2_{g,\beta}} \begin{bmatrix} v_{g,\alpha} & -v_{g,\beta} \\ v_{g,\beta} & v_{g,\alpha} \end{bmatrix} \begin{bmatrix} p^* \\ q^* \end{bmatrix} \tag{5.4}$$

It is important to point out that, in a single-phase system, only the α component of the current is controlled. For this purpose, according to the Eq.5.4, the α and β components of the grid voltage are needed. However, while in three-phase systems they are obtained from the Clarke transformation, in a single-phase system they must be generated by a second order generalized integrator (SOGI). Once the reference of the grid current positive-sequence is obtained, the grid current control is achieved by a proportional resonant (PR) controller. It has a pair of poles on the imaginary axis at the frequency of the sinusoidal waveform that is wished to track, which in this case is the grid frequency.

In the end, the control loop produces the reference of the output inverter voltage. However, as it is well known, the output voltage waveform of a switching power converter can't vary continuously, but it can only assume a certain number of discrete values. As a result, the use of a modulation technique is required in order to drive the switches of each sub-module in such a way that the voltage reference is well tracked. In particular, the nearest-level control (NLC) modulation strategy has been implemented.

The basic concept of the NLC is to approximate the reference of the output inverter voltage with the closest integer voltage level that can be generated by the

CHB, referred to as $N^*{}_V$,[21]. Hence, $N^*{}_V$ can only assume integer values between -N and N.
Subsequently, a sorting algorithm decides which SMs should be inserted or bypassed, in order to achieve the desired voltage level. Traditionally, the sorting algorithm aims to balance the voltages across the SM. The flowchart in Fig.5.4 shows the sorting algorithm implemented. The algorithm is run through at a constant frequency of 1 kHz.

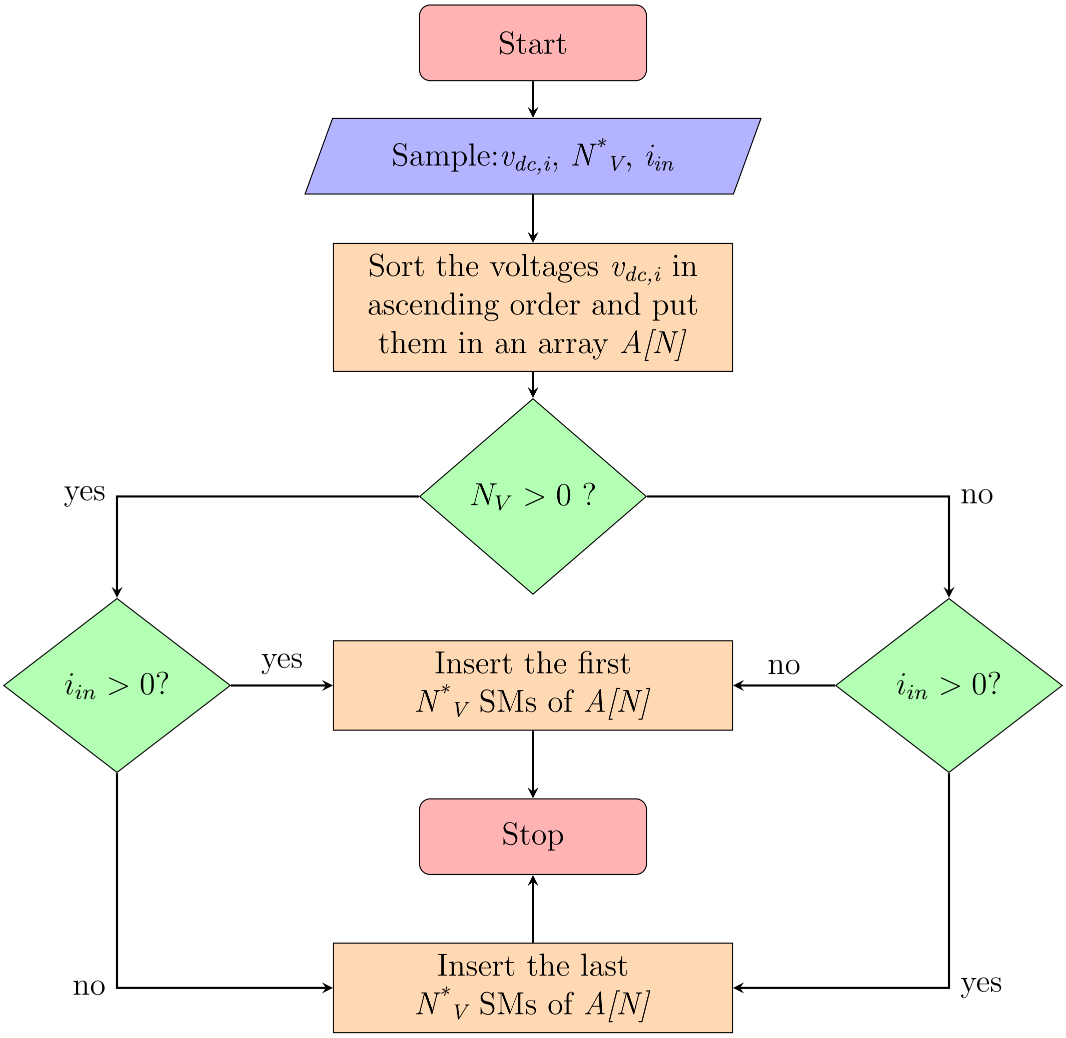

Figure 5.4: Flowchart of the sorting algorithm.

Firstly, the reference level of the output inverter voltage $N^*{}_V$, the current flowing into the CHB i_{in} and all the SM dc-link voltages $v_{dc,i}$ (for $i = 1,...,N$) are sampled. Secondly, the N dc-link voltages are sorted in ascending order. Finally, if through the CHB a discharging current is flowing, then the SMs with the higher voltages are inserted. One the contrary, when a charging current flows through the capacitors, the SMs with the lowest voltages are inserted.
In Fig.5.5 the performance of the sorting algorithm is proved. As can be noticed, all the SM dc-link voltage waveforms are well balanced. In particular, in Fig.5.5(a) all the PV modules are supposed to operate at STC. Whereas, in Fig.5.5(b) only one of them is supposed to receive an irradiance of 100 W/m2.
The main advantage of the sorting algorithm used is represented by the simplicity

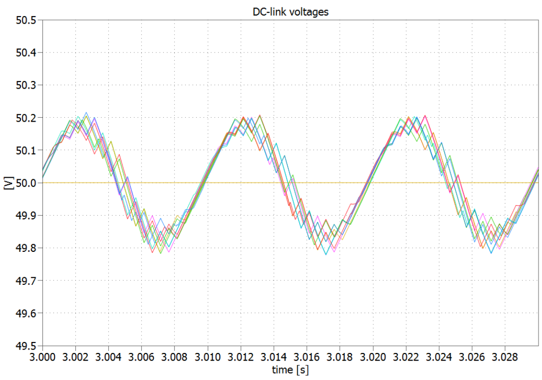

(a)

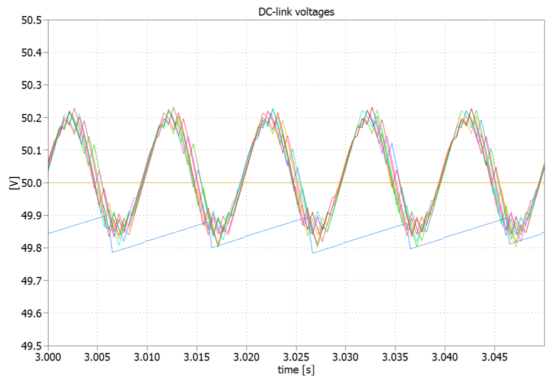

(b)

Figure 5.5: SM capacitor voltages resulting from the sorting algorithm (a)under uniform irradiance conditions; (b) when one PV module is partially shaded.

of its implementation. However, often the switching occurrences are not truly necessary, because they involve the swap of two SMs which have very similar voltages. As a result, this procedure does not represent the best option with respect to the switching losses.

5.3 Simulation Results

In order to show the benefits of the integration of a BESS in a PV CHB-based system, two simulations are run. In the first case, the system without batteries has been considered, like the one shown in Fig.1.5. In the second case, the BESS is inserted at sub-module level, as shown in Fig.5.2.

5.3.1 PV-CHB System Simulation

Two conditions have been considered:

1. All the PV panels are supposed to operate under uniform STC.
2. The irradiance is set equal to 100 W/m2 only for one PV module, while the others are supposed to operate at STC.

In Fig.5.6 the grid current is shown in the two cases.

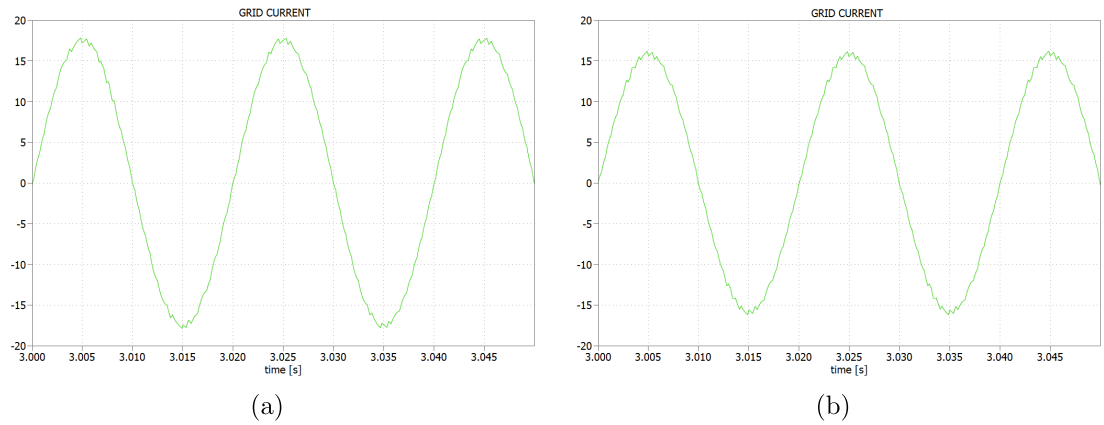

Figure 5.6: Grid current (a)under uniform irradiance conditions; (b) when one PV module is partially shaded.

From the simulation, it follows that, as a consequence of the partial shading involving one PV module, the active power injected into the grid is reduced by around 300 W. However, the others PV modules keep on operating at their MPP. This is one of the main advantages of exploiting a modular dual-stage power converter, with respect to the traditional centralized inverter.

5.3.2 PV-BESS-CHB System Simulation

At the beginning all the PV modules are supposed to operate at STC. Then, only of them is suddenly shaded, and its irradiance value is supposed to drop from 1000 W/m2 to 100 W/m2 in $t = 3\,\text{s}$.

In Fig.5.7 the grid current and the grid power are shown. The time axis is centered around $t = 3\,\text{s}$. As can be noticed, the power grid is not affected by the irradiance variation involving a single PV module. In fact, as can be seen in Fig.5.8(a), the BESS module coupled with the shaded panel, reacts in order to compensate the missing production.

As a drawback, the SOC of the battery related to the shaded module diverges from the others.

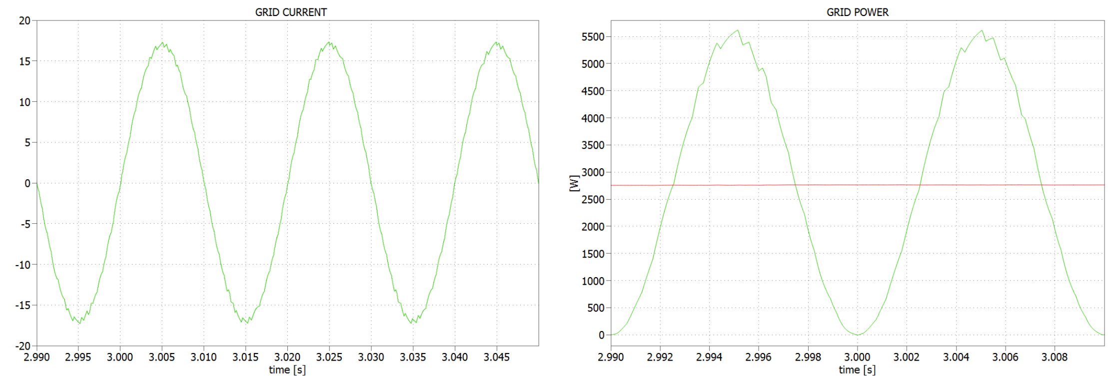

(a) (b)

Figure 5.7: Sudden irradiance change on a single PV module in t=3s (a) Grid current; (b) Grid power.

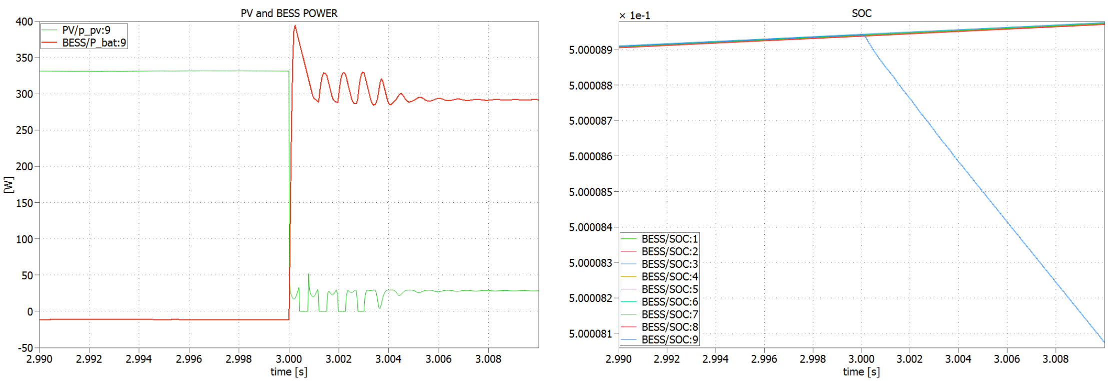

(a) (b)

Figure 5.8: Sudden irradiance change in t=3s (a) PV power and BESS power of the shaded module; (b) SOC of all the BESS modules.

Chapter 6

Conclusions and Future Works

In this project a PV CHB-based system with storage capability provided by batteries has been investigated. Two different topologies for the PV-BESS active power cell have been proposed and compared:

- Topology A: the BESS module is interfaced with the dc-link by means of a dc-dc converter.
- Topology B: the BESS module is directly connected to the sub-module dc-link.

From the comparison can be concluded that:

- The topology A gives more flexibility to the structure, since it allows to independently manage the power provided by each PV-BESS cell.
- The topology A provides a better control of the battery current, which also results in a limitation of the battery internal losses.
- The topology B achieves an higher efficiency. In particular, the European efficiency results to be higher by 2.2 percentage points with respect to the topology A.

In the end, the topology B seems to be promising in a multilevel architecture. However, the control strategy of the whole systems shall be properly designed, with a specific focus on the battery power control and SOC balancing. The design of this control strategy proved to be challenging. For this reason, the topology A has been considered for the simulation of an hybrid PV-BESS CHB-based system. In fact, in this case, the traditional control techniques for multilevel converters can be used. In particular, the CHB has been driven according to a NLC modulation based on a sorting algorithm which operates in order to keep balanced all the SM capacitor voltages.
Form the numerical analysis results that, when a single PV module is affected by a sudden variation of the irradiance level, the BESS coupled with it reacts, by compensating the missing production. As a result, any change is registered in the waveform of the power injected into the grid.

In the future, more suitable balancing algorithm based on the SOC should be investigated, in order to enhance the performance of the proposed architecture, and to ensure a permanent operation of the system. Furthermore, its feasibility must be tested by building a laboratory prototype.

Bibliography

[1] IRENA, "Solar energy data." https://public.tableau.com/shared/YW39WYCWH?:tolbar=no&:display_count=no&:showVizHome=no.

[2] S. Energy, "Global market outlook." http://www.solarpowereurope.org/wp-content/uploads/2018/09/Global-Market-Outlook-2018-2022.pdf, 2018.

[3] S. B. Kjaer, J. K. Pedersen, and F. Blaabjerg, "A review of single-phase grid-connected inverters for photovoltaic modules," *IEEE transactions on industry applications*, vol. 41, no. 5, pp. 1292–1306, 2005.

[4] S. Kouro, J. I. Leon, D. Vinnikov, and L. G. Franquelo, "Grid-connected photovoltaic systems: An overview of recent research and emerging pv converter technology," *IEEE Industrial Electronics Magazine*, vol. 9, no. 1, pp. 47–61, 2015.

[5] U. Sohail, H. Nademi, and L. E. Norum, "A reliable modular based pv-battery hybrid system with peak shaving capability," in *2018 IEEE 19th Workshop on Control and Modeling for Power Electronics (COMPEL)*, pp. 1–6, IEEE, 2018.

[6] L. Zhang, Z. Zhang, J. Qin, D. Shit, and Z. Wang, "Design and performance evaluation of the modular multilevel converter (mmc)-based grid-tied pv-battery conversion system," in *2018 IEEE Energy Conversion Congress and Exposition (ECCE)*, pp. 2649–2654, IEEE, 2018.

[7] SolarEdge, "Se5000-xxs/se6000-xxs." https://www.solaredge.com/sites/default/files/se_storedge_inverter_datasheet_eng.pdf.

[8] S. Ilango, R. V. Nair, R. Chattopadhyay, and S. Bhattacharya, "Photovoltaic and energy storage grid integration with fully modular architecture using triple port active bridges and cascaded h-bridge inverter," in *IECON 2018-44th Annual Conference of the IEEE Industrial Electronics Society*, pp. 1400–1405, IEEE, 2018.

[9] M. Coppola, F. Di Napoli, P. Guerriero, D. Iannuzzi, S. Daliento, and A. Del Pizzo, "An fpga-based advanced control strategy of a gridtied pv chb inverter," *IEEE Transactions on Power Electronics*, vol. 31, no. 1, pp. 806–816, 2016.

[10] F. Di Napoli, M. Coppola, P. Guerriero, D. Iannuzzi, and S. Daliento, "Effective control strategy for photovoltaic cascaded h-bridge inverters developed on fpga platform," in *2015 11th Conference on Ph. D. Research in Microelectronics and Electronics (PRIME)*, pp. 49–52, IEEE, 2015.

[11] P. Guerriero, M. Coppola, F. Di Napoli, G. Brando, A. Dannier, D. Iannuzzi, and S. Daliento, "Three-phase pv chb inverter for a distributed power generation system," *Applied Sciences*, vol. 6, no. 10, p. 287, 2016.

[12] F. Blaabjerg, *Control of Power Electronic Converters and Systems*, vol. 2. Academic Press, 2018.

[13] C. Modules. file:///c:/SAM/2018.11.11/libraries/.

[14] M. Mi, *Hybrid electric vehicles: principles and applications with practical perspectives*. John Wiley & Sons, 2017.

[15] PVGIS. `http://re.jrc.ec.europa.eu/pvg_tools/en/tools.html`.

[16] R. W. Erickson and D. Maksimovic, *Fundamentals of power electronics*. Springer Science & Business Media, 2007.

[17] R. Teodorescu, M. Liserre, and P. Rodriguez, *Grid converters for photovoltaic and wind power systems*, vol. 29. John Wiley & Sons, 2011.

[18] T. M. U. Mohan, Ned and W. P. Robbins, *Power electronics: converters, applications, and design*. John Wiley & Sons, 2003.

[19] PLECS, "User manual ver.4.2. available: https://www.plexim.com/files/plecsmanual.pdf," 2018.

[20] L. S. Xavier, V. M. R. de Jesus, A. F. Cupertino, V. F. Mendes, and H. A. Pereira, "Novel adaptive saturation scheme for photovoltaic inverters with ancillary service capability," in *2017 IEEE 8th International Symposium on Power Electronics for Distributed Generation Systems (PEDG)*, pp. 1–8, IEEE, 2017.

[21] K. Sharifabadi, L. Harnefors, H.-P. Nee, S. Norrga, and R. Teodorescu, *Design, control, and application of modular multilevel converters for HVDC transmission systems*. John Wiley & Sons, 2016.